

# THE COMPLETE INFRARED VIEW OF ACTIVE GALACTIC NUCLEI FROM THE 70-MONTH *SWIFT*/BAT CATALOG

KOHEI ICHIKAWA<sup>1,2,3</sup>, CLAUDIO RICCI<sup>4,5</sup>, YOSHIHIRO UEDA<sup>6</sup>, KENTA MATSUOKA<sup>6</sup>, YOSHIKI TOBA<sup>7</sup>, TAIKI KAWAMURO<sup>6</sup>, BENNY TRAKHTENBROT<sup>8</sup>, AND MICHAEL J. KOSS<sup>8</sup>

<sup>1</sup>National Astronomical Observatory of Japan, 2-21-1 Osawa, Mitaka, Tokyo 181-8588, Japan

<sup>2</sup>Department of Physics and Astronomy, University of Texas at San Antonio, One UTSA Circle, San Antonio, TX 78249, USA

<sup>3</sup>Department of Astronomy, Columbia University, 550 West 120th Street, New York, NY 10027, USA

<sup>4</sup>Institute of Astrophysics, Pontificia Universidad Catolica de Chile, Avenida Vicua Mackenna 4860, 7820436, Chile

<sup>5</sup>Kavli Institute for Astronomy and Astrophysics, Peking University, Beijing 100871, China

<sup>6</sup>Department of Astronomy, Kyoto University, Kitashirakawa-Oiwake-cho, Sakyo-ku, Kyoto 606-8502, Japan

<sup>7</sup>Academia Sinica Institute of Astronomy and Astrophysics, P.O. Box 23-141, Taipei 10617, Taiwan

<sup>8</sup>Institute for Astronomy, Department of Physics, ETH Zurich, Wolfgang-Pauli-Strasse 27, CH-8093 Zurich, Switzerland

## ABSTRACT

We systematically investigate the near- (NIR) to far-infrared (FIR) photometric properties of a nearly complete sample of local active galactic nuclei (AGN) detected in the *Swift*/Burst Alert Telescope (BAT) all-sky ultra hard X-ray (14–195 keV) survey. Out of 606 non-blazar AGN in the *Swift*/BAT 70-month catalog at high galactic latitude of  $|b| > 10^\circ$ , we obtain IR photometric data of 604 objects by cross-matching the AGN positions with catalogs from the *WISE*, *AKARI*, *IRAS*, and *Herschel* infrared observatories. We find a good correlation between the ultra-hard X-ray and mid-IR (MIR) luminosities over five orders of magnitude ( $41 < \log(L_{14-195}/\text{erg s}^{-1}) < 46$ ). Informed by previous measures of the intrinsic spectral energy distribution of AGN, we find FIR pure-AGN candidates whose FIR emission is thought to be AGN-dominated with low starformation activity. We demonstrate that the dust covering factor decreases with the bolometric AGN luminosity, confirming the luminosity-dependent unified scheme. We also show that the completeness of the *WISE* color-color cut in selecting *Swift*/BAT AGN increases strongly with 14–195 keV luminosity.

*Keywords:* galaxies: active — galaxies: nuclei — infrared: galaxies

## 1. INTRODUCTION

Understanding the cosmic evolution of supermassive black holes (SMBHs) in galactic centers and their connections with the evolution of their host galaxies is one of the main goals in modern astronomy. Active galactic nuclei (AGN) are the fundamental laboratories in those studies because they are in the stage where the surrounding gas is accreting onto the SMBHs by releasing their gravitational energy into radiation. It is known that the central engines of AGN are surrounded by a dusty “torus” (Krolik & Begelman 1986). Since optical and ultraviolet emission is easily absorbed by the torus, a complete survey of AGN including obscured populations is crucial to elucidate the growth history of SMBHs.

The ultra-hard X-ray ( $E > 10$  keV) band is extremely useful for detecting the whole population of AGN be-

cause they have 1) stronger penetrating power than optical/UV and even hard ( $E < 10$  keV) X-ray radiation and 2) very little contamination from the starburst emission. Ultra-hard X-ray detectors such as *Swift*/Burst Alert Telescope (BAT, Barthelmy et al. 2005), IBIS/ISGRI on board *INTEGRAL* (Winkler et al. 2003), FPMA/FPMB on board *NuSTAR* (Harrison et al. 2013) are therefore well suited for those studies. Among them, *Swift*/BAT provides the most sensitive ultra-hard X-ray survey of the whole sky in the 14–195 keV range.

Since most of the *Swift*/BAT sources are local objects, they have been observed by a large number of multi-wavelength facilities, which allow us to study their properties. Follow-up studies below 10 keV have shown that the fraction of obscured ( $N_{\text{H}} \geq 10^{22}$  cm<sup>-2</sup>) AGN highly depends on the intrinsic X-ray luminosities (e.g., Beckmann et al. 2009; Burlon et al. 2011; Ricci et al. 2014; Kawamuro et al. 2016a), and also proved to be an effective tool to identify previously missed class of AGN with small opening angle tori (e.g., Ueda et al. 2007; Winter

et al. 2009; Eguchi et al. 2009, 2011; Ricci et al. 2011), and Compton-thick AGN (Gandhi et al. 2015; Ricci et al. 2015; Tanimoto et al. 2016). Studies carried out by optical spectroscopy enable us to investigate the properties of extended ( $> 100$  pc) narrow line regions (NLR; e.g., Hainline et al. 2013, 2014a) through analysis of the [OIII] $\lambda$ 5007 emission line (Winter et al. 2009; Ueda et al. 2015) and also offer the opportunity to estimate the black hole masses through the broad line regions or velocity dispersion measurements. *Swift*/BAT AGN Spectroscopic Survey (BASS) is in progress to complete the first large ( $> 500$ ) sample of BAT detected AGN with optical spectroscopy, which enables us to constrain the nature of the NLR (Koss et al. 2016; Berney et al. 2015; Oh et al. 2016).

Cross-matching the *Swift*/BAT AGN with all-sky mid-infrared (MIR<sup>1</sup>) catalogs can provide information on the dust surrounding the central engine. While sometimes the MIR suffers contamination from the star formation, for luminous AGN the MIR is dominated by the torus dust re-emission with  $T \sim 200$ – $300$  K. This fact is used for new diagnostics identifying various AGN population (Matsuta et al. 2012), and it has shown that clumpy torus models (e.g., Nenkova et al. 2002, 2008a,b; Hönig et al. 2006; Hönig & Kishimoto 2010; Kawaguchi & Mori 2010, 2011; Schartmann et al. 2008; Stalevski et al. 2012; Siebenmorgen et al. 2015) are favored to explain that MIR emission of AGN is almost isotropic (Mullaney et al. 2011; Ichikawa et al. 2012a; Asmus et al. 2015; García-Bernete et al. 2016) rather than the smooth torus models (Pier & Krolik 1992, 1993; Efstathiou & Rowan-Robinson 1995).

Near-IR (NIR) observations ( $\lambda < 5 \mu\text{m}$ ) are useful for identifying luminous obscured AGN because the NIR colors trace well the hot dust emission which cannot be reproduced by starburst galaxies (Lacy et al. 2004; Stern et al. 2005; Hickox et al. 2007; Imanishi et al. 2010; Mateos et al. 2012; Donley et al. 2012; Stern et al. 2012; Assef et al. 2013; Ichikawa et al. 2014). However, the color-color plots often miss the known X-ray selected obscured/Compton-thick AGN due to the strong contamination from the host galaxies in the NIR bands (e.g., Gandhi et al. 2014, 2015), especially at the low-luminosity end (Kawamuro et al. 2016b). Thus we are motivated to evaluate the NIR two-color selection efficiency as a function of AGN luminosity, using a complete sample including Compton-thick and low-luminosity AGN.

On the other hand, far-IR (FIR;  $\lambda \geq 60 \mu\text{m}$ ) data shed light on the starburst emission in the host galaxies of AGN. Using IR Astronomical Satellite (*IRAS*) FIR bands, Rodriguez Espinosa et al. (1987) found that the FIR  $60 \mu\text{m}$  to  $100 \mu\text{m}$  colors of nearby AGN and starburst galaxies are indistinguishable, suggesting that most of the FIR emission of nearby AGN must originate from star formation processes (see also; Netzer et al. 2007; Mullaney et al. 2011). Using the clumpy torus model, Ichikawa et al. (2015) demonstrated that torus model emission is one order of magnitude smaller than the observed *Herschel*  $70 \mu\text{m}$  data points, suggesting starburst emission is necessary in order to reproduce them. Utilizing *Herschel*/PACS  $70/160 \mu\text{m}$  bands, Meléndez et al. (2014) and Mushotzky et al. (2014) found that the FIR emission of most AGN is dominated by the nuclear starburst within the  $\sim 2$  kpc scale, while there are exceptions in which the emission is dominated by the AGN torus (e.g., Matsuoka & Woo 2015; García-González et al. 2016). Hatziminaoglou et al. (2010) also found that the *Spitzer*/MIPS and *Herschel*/SPIRE two-color plot ( $f_{250}/f_{70}$  and  $f_{70}/f_{24}$ ) can separate AGN and starburst galaxies because the  $24 \mu\text{m}$  flux is dominated by the torus emission. However, the SPIRE colors alone do not differ from those of non-AGN galaxies. Thus, combining the MIR and FIR as well as the hard X-ray band enables us to investigate the properties of torus, host galaxies, and accretion processes in AGN, all of which are the key components to understand SMBH/host galaxy connection.

We report here the NIR to FIR ( $3$ – $500 \mu\text{m}$ ) properties of ultra-hard X-ray selected AGN from the *Swift*/BAT 70-month catalog (Baumgartner et al. 2013), by cross-matching the AGN positions with the *WISE*, *AKARI*, *IRAS* all-sky surveys as well as the *Herschel* archived data. The main advantage of the BAT 70 month survey compared to previous *Swift*/BAT surveys includes better sensitivity resulting from a complete reprocessing of the data with an improved data reduction pipeline and more exposure time. Throughout the paper, we adopt  $H_0 = 70.0 \text{ km s}^{-1} \text{ Mpc}^{-1}$ ,  $\Omega_M = 0.3$ , and  $\Omega_\Lambda = 0.7$ .

## 2. SAMPLE

### 2.1. *Swift*/BAT Hard X-ray Catalog

Our initial sample contains the 834 AGN reported in the 70-month *Swift*/BAT catalog (Baumgartner et al. 2013; Ricci et al. 2016b), of which 105 are blazars. Blazars were identified based on the Rome BZCAT (Massaro et al. 2015) and on recent literature (Ricci et al. 2016b). Of the remaining 729 sources, 697 sources have secure redshift information as presented in Ricci et al. (2016b). Next, we removed galaxy pairs or interacting galaxies not resolved in the BAT survey because the

<sup>1</sup> Here we define near-IR (NIR) as  $\lambda < 5 \mu\text{m}$  and MIR as  $5 \mu\text{m} < \lambda \leq 25 \mu\text{m}$  since all of the all-sky IR surveys used here cover IR bands in  $5 \mu\text{m} < \lambda \leq 25 \mu\text{m}$ , whereas only the *WISE* survey covers IR bands at  $\lambda < 5 \mu\text{m}$ .

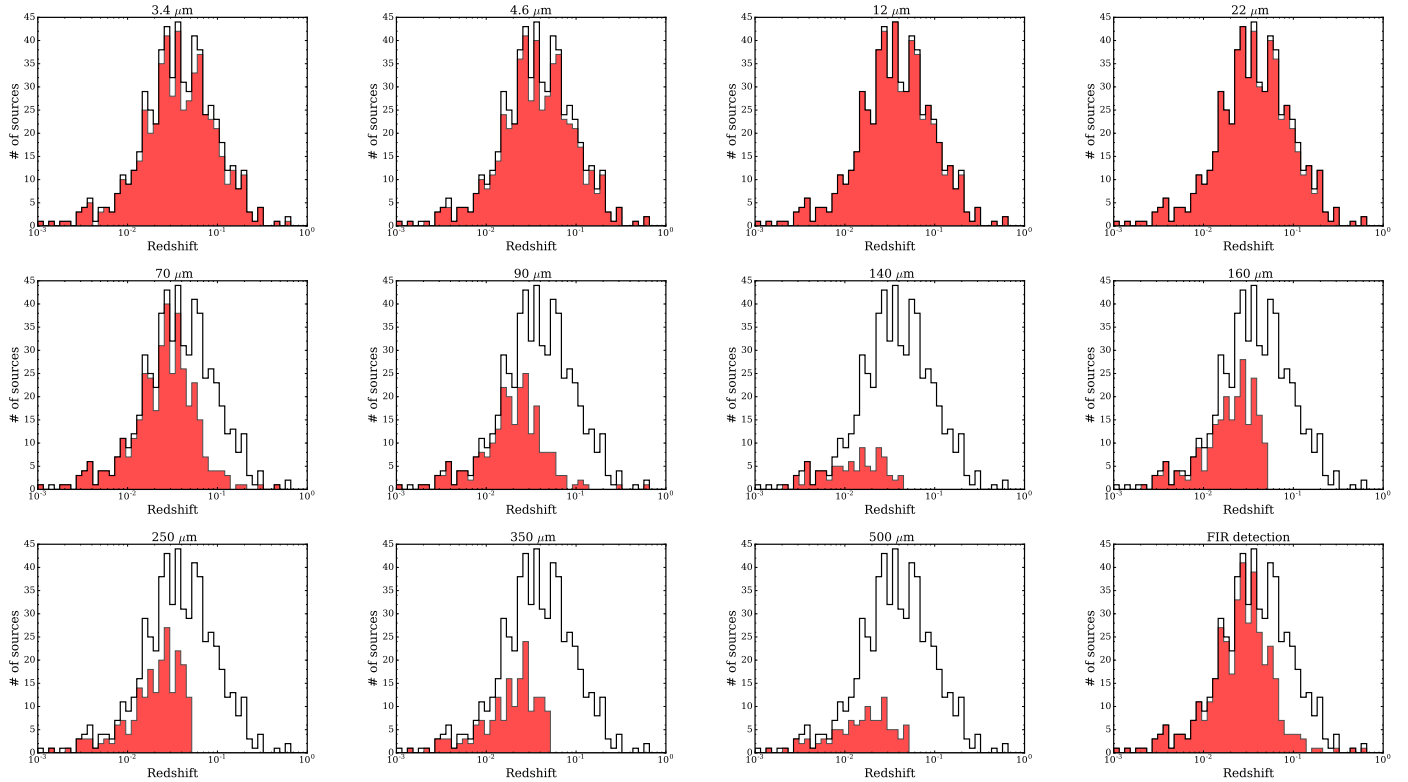


**Figure 1.** Redshift distribution of AGN in the *Swift*/BAT 70-month catalog (black solid line: 606 objects) and of those with IR counterparts (red color area) at each wavelength. “FIR detection” represents the counterparts detected in any of the FIR bands. The number of detected sources at each IR band is compiled in Table 2.

BAT catalog in [Baumgartner et al. \(2013\)](#) only provides the counterpart name of the galaxy pair, not the galaxy itself, which makes us to obtain the IR counterpart very difficult for those sources. Out of 697 sources, 684 fulfilled this criterion. Further, the 606 sources located at higher galactic latitude with  $|b| > 10^\circ$  were selected to reduce the contamination in the crowded region through IR catalog matching. In the following we refer only to these 606 non-blazar AGN as the parent sample. The sample is local, with an average redshift of  $\langle z \rangle = 0.055$  as shown in Figure 1 (black solid lines)<sup>2</sup>. [Ricci et al. \(2016b\)](#) collected the X-ray spectra below 10 keV, including the  $\sim 60$  unknown objects in the *Swift*/BAT 70-month catalog, then derived the best estimated line of sight column density ( $N_{\text{H}}$ ) and absorption corrected BAT 14–195 keV luminosity ( $L_{14-195}$ ). Even the energy band of the *Swift*/BAT survey, the observed flux is affected by obscuring material if the column density of the target exceeds  $N_{\text{H}} > 10^{24} \text{ cm}^{-2}$  (e.g., see Figure 1 of [Ricci et al. 2015](#)). Thus, we use absorption corrected 14–195 keV luminosity ( $L_{14-195}$ ) in this study and all

<sup>2</sup> M 81 is not shown in the Figures due to its low redshift ( $z < 10^{-3}$ ).

the values of  $L_{14-195}$  and  $N_{\text{H}}$  will be tabulated in [Ricci et al. \(2016b\)](#).

## 2.2. IR Catalogs

The available NIR to FIR data were obtained as follows.

### 2.2.1. ALLWISE Catalog

The *WISE* mission mapped the all-sky in 3.4 (W1), 4.6 (W2), 12 (W3), and 22  $\mu\text{m}$  (W4) bands. In this study, we obtained the data from the latest ALLWISE catalog ([Cutri et al. 2013](#)) that achieved better sensitivity than the *WISE* all-sky data release ([Wright et al. 2010](#)) thanks to an improved data processing pipeline. The catalog tabulates the pipeline-measured magnitudes based on the profile fitting on  $\sim 6$  arcsec scale. In this study, we use this instrumental profile-fit photometry magnitude. The ALLWISE achieved  $5\sigma$  sensitivity at 3.4, 4.6, 12, and 22  $\mu\text{m}$  is 0.054, 0.071, 1, and 6 mJy, respectively. The positional accuracy based on cross-matching with the 2MASS catalog is  $\sim 2$  arcsec at  $3\sigma$  level. We only use the sources with the flux quality `ph_qual=A`, with a signal-to-noise ratio larger than 10. We also check sources of contamination and/or biased flux, due to the proximity to an image artifact (e.g., diffraction spikes, scattered-light halos, and/or optical ghosts) us-

ing the flag name `ccflag`. A source that is unaffected by known artifacts is flagged as `ccflag=0`. We thus only use sources with `ccflag=0` for each band.

### 2.2.2. *AKARI Point Source Catalogs*

To further obtain the IR properties of the *Swift*/BAT AGN, we use the *AKARI* All-Sky Survey Point Source Catalogs (AKARI-PSC). *AKARI* carries two instruments, the infrared camera (IRC; Onaka et al. 2007) operating in the 2–26  $\mu\text{m}$  band (centered at 9  $\mu\text{m}$  and 18  $\mu\text{m}$ ) and the Far-Infrared Surveyor (FIS; Kawada et al. 2007) operating in the 50–200  $\mu\text{m}$  band (centered at 65, 90, 140, and 160  $\mu\text{m}$ ). The *AKARI* catalogs cover the brightest sources ( $> 1$  Jy at 12  $\mu\text{m}$  band) whose fluxes ALLWISE could not trace properly due to saturation. The AKARI-PSC achieved the flux sensitivities of 0.05, 0.09, 2.4, 0.55, 1.4, and 6.3 Jy with position accuracies of 6 arcsec at the 9, 18, 65, 90, 140, and 160  $\mu\text{m}$  bands, respectively. In our study, we only utilize sources with the quality flag of `fqual=3`, whose flux measurements are reliable<sup>3</sup>.

### 2.2.3. *IRAS Catalogs*

The *IRAS* mission performed an unbiased all sky survey in the 12, 25, 60, and 100  $\mu\text{m}$  bands. The typical position accuracy at 12 and 25  $\mu\text{m}$  is 7 arcsec and 35 arcsec in the scan and cross scan direction, respectively (Beichman et al. 1988). In this paper we use two largest catalogs, the *IRAS* Point Source Catalog (*IRAS*-PSC) and the *IRAS* Faint Source Catalog (*IRAS*-FSC). *IRAS* achieved  $10\sigma$  point source sensitivities better than 0.7 Jy over the whole sky. The *IRAS*-FSC contains even fainter sources with fluxes of  $>0.2$  Jy in the 12 and 25  $\mu\text{m}$  bands. We use only *IRAS* sources with `fqual=3` (the highest quality)<sup>4</sup>.

### 2.2.4. *Herschel BAT AGN Catalog*

The *Swift*/BAT AGN were also observed with *Herschel*/Photodetector Array Camera and Spectrometer (PACS; Poglitsch et al. 2010) and Spectral and Photometric Imaging Receiver (SPIRE; Griffin et al. 2010). Meléndez et al. (2014) compiled a catalog of 313 nearby ( $z < 0.05$ ) sources observed with *Herschel*/PACS. The PACS covers the two bands at the center wavelength of 70  $\mu\text{m}$  (60–85  $\mu\text{m}$ ) and 160  $\mu\text{m}$  (130–210  $\mu\text{m}$ ) simultaneously. The PSF is 1.4 and 2.85 arcsec at 70  $\mu\text{m}$  and

160  $\mu\text{m}$ , respectively. Considering the median redshift ( $z \sim 0.025$ ) of the catalog, PACS 70  $\mu\text{m}$  PSF covers  $\sim 2.8$  kpc, which contains most of the host galaxy component. Shimizu et al. (2016) reported that nearby ( $z < 0.05$ ) 293 sources were observed with *Herschel*/SPIRE as part of a cycle-1 open time program. In addition, other 20 sources were included from other separate programs to complete the sample. The PSF is 18, 24, and 36 arcsec for 250, 350, and 500  $\mu\text{m}$ , respectively.

## 2.3. *Cross Matching of BAT AGN with the IR Catalogs*

We first compile the IR counterparts by cross matching the BAT AGN positions with IR catalogs. In this study, the IR luminosity  $L_{X \mu\text{m}}$  represents the observed frame luminosity  $\lambda L_{\lambda}(X \mu\text{m})$  ( $\text{erg s}^{-1}$ ), where  $3.4 \leq X \leq 500$ .

### 2.3.1. *NIR bands*

We determine the NIR (3.4 and 4.6  $\mu\text{m}$ ) counterparts of the *Swift*/BAT AGN through the positional matching with the ALLWISE. We applied a cross-matching radius of 2 arcsec, informed by the cross-matches with the 2MASS catalog as described in Section 2.2.1. Using ALLWISE, we found 591 NIR counterparts out of 606 sources within the 2 arcsec radius. Considering the superb sensitivity of ALLWISE than that of the BAT survey (see Appendix A), essentially all of them should be detected. Therefore, we checked again the ALLWISE counterparts of the remaining 15 non-detected sources by expanding the matching-radius. As a result, 13 sources have been found within 5 arcsec radius, and we confirmed that the detections are real based on the visual inspection of DSS optical and ALLWISE images. One of the remaining two sources not detected, the counterpart of NGC 3516 was classified as one of the ALLWISE reject table sources<sup>5</sup>. Another source (3C 59) was not detected even by expanding the searching radius up to 15 arcsec. After checking the visual inspection between DSS optical and XMM/PN X-ray image, we found that the coordinate of 3C 59 in the BAT catalog traces the jet lobe component, not the central object. We used the coordinate of the central object obtained from Simbad (RA, Dec)=(31.7592, 29.512775) for this target and we found the *WISE* counterpart successfully. In total, 605 counterparts are identified in the ALLWISE catalog.

Out of the 605 sources, 602 and 603 sources fulfill `ph_qual=A` at 3.4  $\mu\text{m}$  and 4.6  $\mu\text{m}$ . After selecting the sources which fulfill `ccflag = 0`, the number of IR counterparts at 3.4  $\mu\text{m}$  and 4.6  $\mu\text{m}$  turns out to be 549

<sup>3</sup> See the release note of the AKARI/FIS catalog for the details of `fqual`. It is recommended not to use the flux data when `fqual <= 2` for a reliable scientific analysis. [http://irsa.ipac.caltech.edu/data/AKARI/documentation/AKARI-FIS\\_BSC\\_V1\\_RN.pdf](http://irsa.ipac.caltech.edu/data/AKARI/documentation/AKARI-FIS_BSC_V1_RN.pdf)

<sup>4</sup> see Beichman et al. (1988) for the definition of `fqual` in the *IRAS* catalogs. False detections may be included when `fqual <= 2`.

<sup>5</sup> The sources not selected from the ALLWISE catalog because they are low signal-to-noise ratio or spurious detections of image artifacts

( $\sim 90.6\%$ ) and 548 ( $\sim 90.4\%$ ) sources, respectively. The number of IR counterparts in the NIR band (either 3.4 or 4.6  $\mu\text{m}$ ) is 560 ( $\sim 92.4\%$ ) sources.

### 2.3.2. MIR bands

We determine the MIR (9–25  $\mu\text{m}$ ) counterparts of the *Swift*/BAT AGN by cross matching the ALLWISE, *AKARI*, and *IRAS* catalogs in this order. Our primary goal is to obtain photometric data in the IR band as completely as possible for the *Swift*/BAT selected AGN. We give the highest priority to the ALLWISE catalog because of its 50 times better sensitivity than *AKARI*, which allows us to search for fainter sources in the MIR all-sky view. Then we cross matched the sources undetected by ALLWISE with *AKARI*. *AKARI* covers the brighter sources which are saturated due to the high sensitivity of ALLWISE, and have the advantage of a 2–4 times higher sensitivity than the *IRAS* survey. While all the *IRAS* sources should be detected with *AKARI*, the flux quality flags of *AKARI* for very nearby ( $z < 0.005$ ) objects turn out to be bad due to their extended morphology when fitted with a single Gaussian. In such cases, we rather refer to the *IRAS* data with good flux quality, which have  $\sim 11$  times worse angular resolution than *AKARI*, since we aim to measure the total MIR flux from both nucleus and host galaxy in a uniform way for the whole AGN sample.

The positional matching of the optical counterparts of the *Swift*/BAT AGN with IR survey catalogs was already discussed in Section 2.3.1 for ALLWISE and in Ichikawa et al. (2012a) for *AKARI* and *IRAS*, and we follow here the same approach. For the MIR bands, the number of detections is compiled at the second column in Table 2. Here the detection at 12  $\mu\text{m}$  represents the detection either at *AKARI* 9  $\mu\text{m}$ , *WISE* 12  $\mu\text{m}$ , or *IRAS* 12  $\mu\text{m}$ ; 22  $\mu\text{m}$  represents either at *AKARI* 18  $\mu\text{m}$ , *WISE* 22  $\mu\text{m}$ , or *IRAS* 25  $\mu\text{m}$ ; the MIR band represents either at 12  $\mu\text{m}$  or 22  $\mu\text{m}$  band defined above. Finally, we obtained 601 ( $\sim 99.2\%$ ) counterparts in at least one MIR band. Thus, the identification in the MIR bands is almost as complete as in the NIR bands. The redshift distribution of the IR counterparts at each wavelength is shown in Figure 1.

### 2.3.3. FIR bands

The FIR counterparts of the *Swift*/BAT AGN at  $60 \leq \lambda \leq 160 \mu\text{m}$  were gathered by cross-matching the *AKARI*, *IRAS*, and *Herschel* in this order. Our goal is to obtain photometric data for the full host galaxy emission in the FIR band. We gave *AKARI* counterparts the highest priority because of the better sensitivity with respect to *IRAS* surveys. Then we matched the portion of the sources undetected by *AKARI* with *IRAS*. Considering the better sensitivity of *AKARI*/FIS, one might

expect that *IRAS* would not cover many sources. However, *AKARI* often misses emission from sources with extended morphology due to its better angular resolution. In such cases, *IRAS* gives the best quality estimate of flux by measuring the whole FIR flux from the host galaxies. Finally, the remaining distant sources or faint sources which neither *AKARI* nor *IRAS* detected were cross matched with the *Herschel*/PACS catalog of Meléndez et al. (2014). We cross matched the sources by referring to the counterpart source names reported by Meléndez et al. (2014) and the *Swift*/BAT catalog.

For the FIR counterpart at  $250 \leq \lambda \leq 500 \mu\text{m}$ , only *Herschel*/SPIRE catalog can access to those wavelengths. We also cross matched the sources by referring the counterpart source names written in Shimizu et al. (2016) and the *Swift*/BAT catalog.

For the FIR bands, 388 ( $\sim 64.2\%$ ), 241 ( $\sim 39.9\%$ ), 89 ( $\sim 14.7\%$ ), 229 ( $\sim 37.9\%$ ), 213 ( $\sim 35.3\%$ ), 170 ( $\sim 28.1\%$ ), and 107 ( $\sim 17.7\%$ ) sources are compiled at 70 (either at *IRAS* 60  $\mu\text{m}$ , *AKARI* 65  $\mu\text{m}$ , or *Herschel* 70  $\mu\text{m}$ ), 90 (either at *AKARI* 90  $\mu\text{m}$  or *IRAS* 100  $\mu\text{m}$ ), 140 (at *AKARI* 140  $\mu\text{m}$ ), and 160  $\mu\text{m}$  (at *Herschel* 160  $\mu\text{m}$  or *AKARI* 160  $\mu\text{m}$ ), 250  $\mu\text{m}$  (at *Herschel*/SPIRE 250  $\mu\text{m}$ ), 350  $\mu\text{m}$  (at *Herschel*/SPIRE 350  $\mu\text{m}$ ), 500  $\mu\text{m}$  (at *Herschel*/SPIRE 500  $\mu\text{m}$ ), respectively. Those numbers are also compiled in the second column of Table 2. Finally, 402 ( $\sim 66.3\%$ ) IR counterparts are obtained in at least one FIR band. Thus, the identification in the FIR bands is not yet complete, but a statistically significant sample has been compiled for this analysis.

## 2.4. Luminosity Correlation among IR catalogs

Since the four IR catalogs have slightly different central wavelengths and aperture sizes, we investigate the correlation between the *AKARI*/*IRAS*/*WISE*/*Herschel* luminosities, using only the sources detected in two separate observations. For the MIR bands, we choose *AKARI* 9  $\mu\text{m}$  and *IRAS* 12  $\mu\text{m}$  for *WISE* 12  $\mu\text{m}$ , and *AKARI* 18  $\mu\text{m}$  and *IRAS* 25  $\mu\text{m}$  for *WISE* 22  $\mu\text{m}$ , respectively, because of the proximity of the central wavelengths. For the FIR bands, *AKARI* 65  $\mu\text{m}$  and *IRAS* 60  $\mu\text{m}$  for *Herschel*/PACS 70  $\mu\text{m}$ , *IRAS* 100  $\mu\text{m}$  for *AKARI* 90  $\mu\text{m}$ , *AKARI* 160  $\mu\text{m}$  for *Herschel*/PACS 160  $\mu\text{m}$ . Figure 2 displays the flux correlations between the two bands, showing that the correlation in flux between different IR catalogs are tight and significant. The standard deviation of the flux-ratio distribution between these two bands are written in the caption of Figure 2.

Figure 2 also shows that the flux relations are independent from the redshift. Although within the scatter, the flux relations between *WISE* 12, 22  $\mu\text{m}$  and *IRAS* 12, 25  $\mu\text{m}$  show systematic  $z$  dependence that flux ratio of  $f_{\text{IRAS}}/f_{\text{WISE}}$  is anti-correlated to  $z$ . This could be due

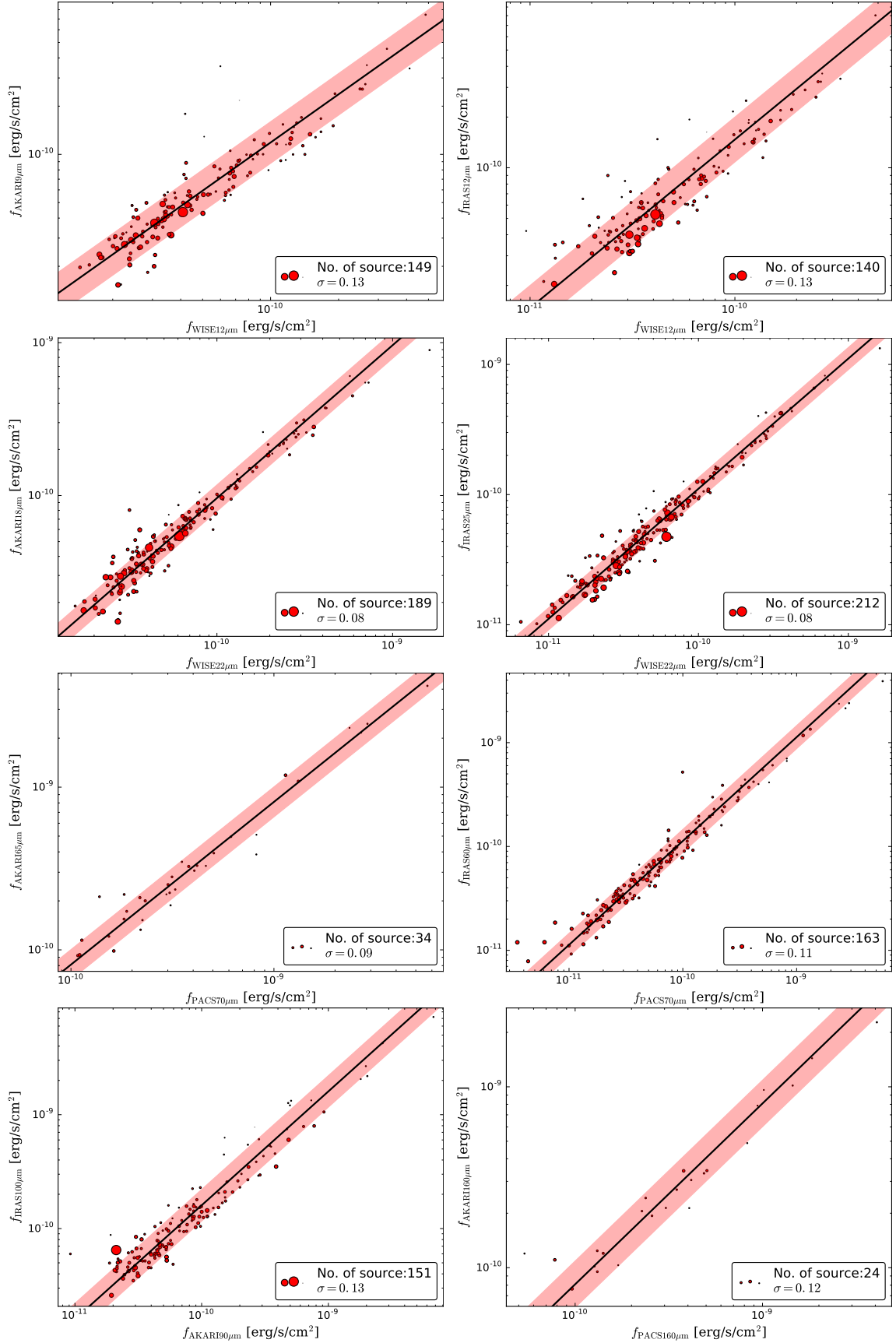


**Figure 2.** Flux-flux relations of AGN between two IR bands. The red color filled circle represents the source detected in both bands. The size of the circle is proportional to the redshift of the source. The solid line represents the best-fit line and red colored shade are represents  $1\sigma$  dispersion of each linear scaling relation. The number of sources for the fitting and  $1\sigma$  error is also written in the right bottom at each panel. (Left) From top to bottom, *AKARI* 9  $\mu\text{m}$  vs. *WISE* 12  $\mu\text{m}$ , *AKARI* 18  $\mu\text{m}$  vs. *WISE* 22  $\mu\text{m}$ , *AKARI* 65  $\mu\text{m}$  vs. *Herschel/PACS* 70  $\mu\text{m}$ , *IRAS* 100  $\mu\text{m}$  vs. *AKARI* 90  $\mu\text{m}$ , (Right) from top to bottom, *IRAS* 12  $\mu\text{m}$  vs. *WISE* 12  $\mu\text{m}$ , *IRAS* 25  $\mu\text{m}$  vs. *WISE* 22  $\mu\text{m}$ , *IRAS* 60  $\mu\text{m}$  vs. *Herschel/PACS* 70  $\mu\text{m}$ , *AKARI* 160  $\mu\text{m}$  vs. *Herschel/PACS* 160  $\mu\text{m}$ .

to greatly larger aperture of *IRAS* than that of *WISE*, therefore the MIR emission from the host galaxy slightly contaminates to the *IRAS* fluxes of low- $z$  sources.

Based on the flux correlation, we derive the empirical formula to convert the flux of each band into *WISE* 12  $\mu\text{m}$ , 22  $\mu\text{m}$ , Herschel/PACS 70  $\mu\text{m}$ , 160  $\mu\text{m}$ , and *AKARI* 90  $\mu\text{m}$  as follows:

$$\begin{aligned} \log\left(\frac{f_{\text{WISE } 12 \mu\text{m}}}{\text{erg s}^{-1} \text{cm}^{-2}}\right) &= \log\left(\frac{f_{\text{AKARI } 9 \mu\text{m}}}{\text{erg s}^{-1} \text{cm}^{-2}}\right) - 0.074 \\ \log\left(\frac{f_{\text{WISE } 12 \mu\text{m}}}{\text{erg s}^{-1} \text{cm}^{-2}}\right) &= \log\left(\frac{f_{\text{IRAS } 12 \mu\text{m}}}{\text{erg s}^{-1} \text{cm}^{-2}}\right) - 0.167 \\ \log\left(\frac{f_{\text{WISE } 22 \mu\text{m}}}{\text{erg s}^{-1} \text{cm}^{-2}}\right) &= \log\left(\frac{f_{\text{AKARI } 18 \mu\text{m}}}{\text{erg s}^{-1} \text{cm}^{-2}}\right) + 0.017 \\ \log\left(\frac{f_{\text{WISE } 22 \mu\text{m}}}{\text{erg s}^{-1} \text{cm}^{-2}}\right) &= \log\left(\frac{f_{\text{IRAS } 25 \mu\text{m}}}{\text{erg s}^{-1} \text{cm}^{-2}}\right) - 0.045 \\ \log\left(\frac{f_{\text{PACS } 70 \mu\text{m}}}{\text{erg s}^{-1} \text{cm}^{-2}}\right) &= \log\left(\frac{f_{\text{AKARI } 65 \mu\text{m}}}{\text{erg s}^{-1} \text{cm}^{-2}}\right) + 0.091 \\ \log\left(\frac{f_{\text{PACS } 70 \mu\text{m}}}{\text{erg s}^{-1} \text{cm}^{-2}}\right) &= \log\left(\frac{f_{\text{IRAS } 60 \mu\text{m}}}{\text{erg s}^{-1} \text{cm}^{-2}}\right) - 0.053 \\ \log\left(\frac{f_{\text{AKARI } 90 \mu\text{m}}}{\text{erg s}^{-1} \text{cm}^{-2}}\right) &= \log\left(\frac{f_{\text{IRAS } 100 \mu\text{m}}}{\text{erg s}^{-1} \text{cm}^{-2}}\right) - 0.204 \\ \log\left(\frac{f_{\text{PACS } 160 \mu\text{m}}}{\text{erg s}^{-1} \text{cm}^{-2}}\right) &= \log\left(\frac{f_{\text{AKARI } 160 \mu\text{m}}}{\text{erg s}^{-1} \text{cm}^{-2}}\right) + 0.092 \end{aligned}$$

Assuming that AGN that are not detected in the highest priority band (*WISE* 12  $\mu\text{m}$ , 22  $\mu\text{m}$ , Herschel/PACS 70  $\mu\text{m}$ , 160  $\mu\text{m}$ , and *AKARI* 90  $\mu\text{m}$ ) but in second or third priority bands should follow the same correlations as examined here, we apply the conversion factors reported above to derive the 12, 22, 70, 90, and 160  $\mu\text{m}$  luminosities. Doing so we can discuss the luminosity correlation with the 14–195 keV band in a uniform way regardless of the matched catalogs. All the IR properties of the parent sample AGN are summarized in Table 1.

### 2.5. AGN type

To examine the IR properties of different AGN populations, we divide the sample into two types based on the column density ( $N_{\text{H}}$ ) obtained from the X-ray spectral fitting by Ricci et al. (2016b). The AGN with  $N_{\text{H}} < 10^{22} \text{ cm}^{-2}$  are called “X-ray type-1” (hereafter type-1), and the AGN with  $N_{\text{H}} \geq 10^{22} \text{ cm}^{-2}$  are called “X-ray type-2” (hereafter type-2). The sample is divided into 311 type-1 AGN and 293 type-2 AGN. The AGN type of each source will be tabulated in Ricci et al. (2016b).

## 3. RESULTS AND DISCUSSION

### 3.1. Correlation between the MIR and Ultra-Hard X-Ray Luminosities

Figure 3 shows the luminosity correlations between the MIR (12 and 22  $\mu\text{m}$ ) luminosities ( $L_{12\mu\text{m}}, L_{22\mu\text{m}}$ ) and  $L_{14-195}$  in the luminosity range of  $10^{40} < L_{14-195} < 10^{47} \text{ erg s}^{-1}$ <sup>6</sup>. Blue and red crosses represent type-1 and type-2 AGN, respectively. The error-bars are not shown in Figure 3 and Figure 4 since the uncertainties of both infrared luminosities and 14–195 keV luminosity are vanishingly small ( $< 10\%$ ) in the log-log plot.

Since our motivation is to determine the slope of the luminosity relation between  $L_{\text{MIR}}$  and  $L_{14-195}$  as two independent variables, we apply ordinary least-squares Bisector fits, which minimizes perpendicular distance from the slope line to data points (Isobe et al. 1990). The ordinal least-squares Bisector fits (with the form of  $[\log(L_{\text{MIR}}/10^{43} \text{ erg s}^{-1}) = (a \pm \Delta a) + (b \pm \Delta b) \log(L_{14-195}/10^{43} \text{ erg s}^{-1})]$ , where  $\Delta a$  and  $\Delta b$  is the standard deviation of  $a$  and  $b$ , respectively) gives the correlations of

$$\log \frac{L_{12\mu\text{m}}}{10^{43} \text{ erg/s}} = (-0.10 \pm 0.02) + (0.96 \pm 0.02) \log \frac{L_{14-195}}{10^{43} \text{ erg/s}} \quad (1)$$

$$\log \frac{L_{22\mu\text{m}}}{10^{43} \text{ erg/s}} = (0.02 \pm 0.02) + (0.98 \pm 0.02) \log \frac{L_{14-195}}{10^{43} \text{ erg/s}} \quad (2)$$

The significance of the correlations between the two bands luminosities (and fluxes) can be obtained by performing Spearman’s tests. The results are summarized in Table 2. We find that both luminosity–luminosity and flux–flux correlations between the NIR, MIR bands and the 14–195 keV bands are highly significant.

In the Seyfert galaxy class with  $L_{14-195} < 10^{44} \text{ erg s}^{-1}$ , the correlation between MIR and X-ray was first reported by using ground telescopes with low spatial resolutions (Elvis et al. 1978; Krabbe et al. 2001), and then by several authors thanks to the new windows opened by the *ISO* satellite (Lutz et al. 2004; Ramos Almeida et al. 2007) and by *Spitzer* (Sazonov et al. 2012). Studies based on the ground-based high spatial resolution MIR photometry were first compiled by Horst et al. (2006), then expanded independently by Levenson et al. (2009) and Gandhi et al. (2009), and finally by Asmus et al. (2015). The correlation parameters of Gandhi et al. (2009) and Asmus et al. (2015) are the most widely used because they include Compton-thick AGN. Gandhi et al. (2009) show steeper results than ours with  $b = 1.11 \pm 0.04$ , but Asmus et al. (2015) report the re-

<sup>6</sup> M 81 and NGC 4395 are not shown in Figure 3 and 4 due to their low luminosities of ( $\log L_{12 \mu\text{m}}, \log L_{22\mu\text{m}}, \log L_{90 \mu\text{m}}, \log L_{14-195}$ ) = (39.20, 39.22, 39.76, 38.50) for M 81 and ( $\log L_{12 \mu\text{m}}, \log L_{22\mu\text{m}}, \log L_{90 \mu\text{m}}, \log L_{14-195}$ ) = (39.88, 40.27, 41.48, 40.77) for NGC 4395.

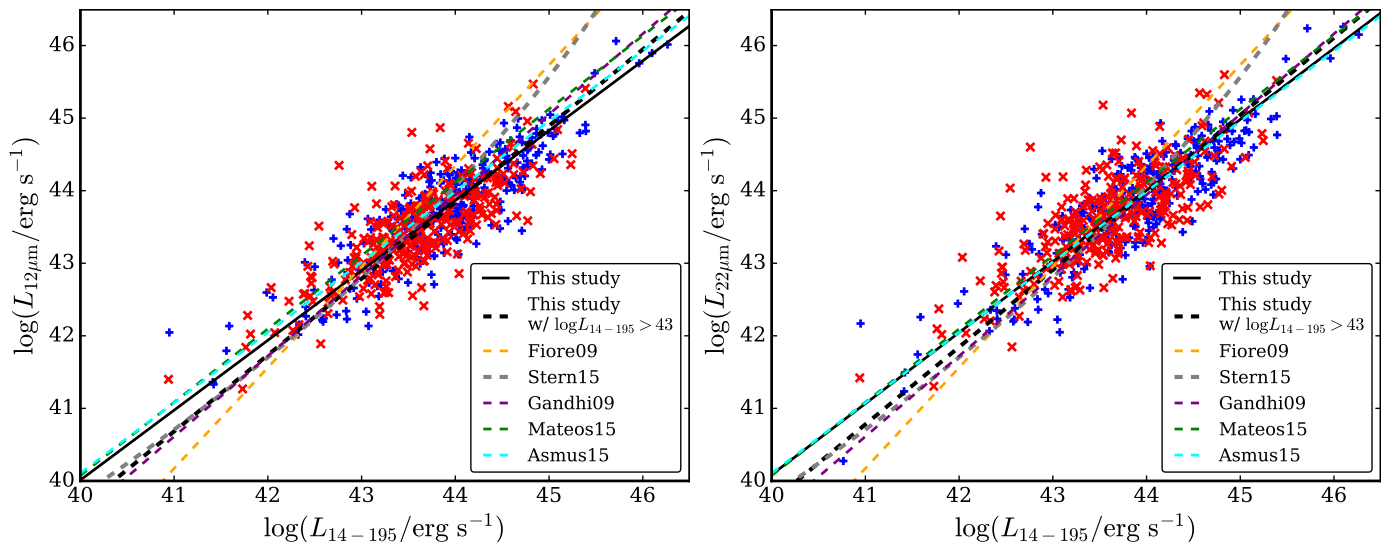


**Figure 3.** Luminosity correlations between the luminosities at 12 (left) and 22  $\mu\text{m}$  (right) ( $L_{12\ \mu\text{m}}, L_{22\ \mu\text{m}}$ ) and 14–195 keV ( $L_{14-195}$ ). Blue/red cross represents type-1/-2, respectively. The black solid line represents the slope of our study in Equation (1) for left panel and (2) for right panel. The black dashed line represents the slope of our study using only high luminosity sources with  $\log L_{14-195} > 43$ . The other dashed line represents the study of [Fiore et al. \(2009\)](#) (orange), [Stern \(2015\)](#) (gray), [Gandhi et al. \(2009\)](#) (purple), [Mateos et al. \(2015\)](#) (green), and [Asmus et al. \(2015\)](#) (cyan) respectively. The studies with local sample (mostly  $z < 0.1$  and main luminosity range of  $41 < L_X < 46$ ) are our study, [Gandhi et al. \(2009\)](#), and [Asmus et al. \(2015\)](#). The studies with high- $z$  sample (mostly  $0.1 < z < 5$  and  $42 < L_X < 46$ ) are [Fiore et al. \(2009\)](#), [Mateos et al. \(2015\)](#), and [Stern \(2015\)](#). The studies with type-1 AGN are [Fiore et al. \(2009\)](#), [Stern \(2015\)](#), and with both type-1 and type-2 AGN are [Gandhi et al. \(2009\)](#), [Mateos et al. \(2015\)](#), [Asmus et al. \(2015\)](#), and our study. See Table 2 for more details.

sults consistent with our studies within the uncertainties with  $b = 0.97 \pm 0.03$ . Both slopes are over-plotted in Figure 3 and also compiled in Table 2. Since both studies used 2–10 keV luminosity as X-ray luminosity, we apply the conversion factor of  $L_{14-195}/L_{2-10} = 2.1$  under the assumption of  $\Gamma = 1.9$  for the over-plot in Figure 3. Hereafter, we always apply this conversion factor for estimating  $L_{14-195}$  from  $L_{2-10}$ .

The host galaxy contamination in the MIR emission especially in the low-luminosity end could affect the slope values of  $b = 0.96 - 0.98$  in our study. If we use only the sources with  $L_{14-195} > 10^{43}$  erg  $\text{s}^{-1}$ , the luminosity relations become

$$\log \frac{L_{12\mu\text{m}}}{10^{43} \text{ erg/s}} = (-0.21 \pm 0.03) + (1.05 \pm 0.03) \log \frac{L_{14-195}}{10^{43} \text{ erg/s}} \quad (3)$$

$$\log \frac{L_{22\mu\text{m}}}{10^{43} \text{ erg/s}} = (-0.09 \pm 0.03) + (1.07 \pm 0.03) \log \frac{L_{14-195}}{10^{43} \text{ erg/s}}, \quad (4)$$

which is slightly steeper, but within  $2\sigma$  uncertainty of [Asmus et al. \(2015\)](#). The slope obtained by [Gandhi et al. \(2009\)](#) depends on the choice of algorithm and the value becomes  $b = 1.00 \pm 0.08$  when using the same method of [Asmus et al. \(2015\)](#). Therefore, our results are generally fully consistent with the high spatial resolution results in high luminosity end with  $L_{14-195} > 10^{43}$  erg  $\text{s}^{-1}$ . While our results with poorer spatial resolution suffer from the contamination from the host galaxies in the

lower luminosity end, our study has the advantage of the completeness ( $\sim 98\%$ ) in the MIR bands of the ultra-hard-X-ray flux limited *Swift*/BAT 70 month catalog, which is the least bias against absorption up to  $N_{\text{H}} \simeq 10^{24}$   $\text{cm}^{-2}$ .

The comparison to the literature from the higher luminosity (and also high- $z$ ) studies with  $L_{14-195} \geq 10^{44}$  erg  $\text{s}^{-1}$  can also provide important information. We compile the luminosity correlations of those studies in Table 3. [Fiore et al. \(2009\)](#) derived the observed rest-frame 6  $\mu\text{m}$  and 2–10 keV luminosities of  $\sim 80$  X-ray-selected type-1 AGN in the COSMOS and CDF-S fields obtained from *Chandra* and *Spitzer* satellites. The slope is quite steep, with  $b = 1.39$  for  $\log(L_{6\ \mu\text{m}}/\text{erg s}^{-1}) \geq 43$ . Although the detailed fitting algorithm were not mentioned in their studies, there is a trend of increasing MIR–X-ray ratio at high luminosity end with  $\log(L_{6\ \mu\text{m}}/\text{erg s}^{-1}) > 44$ . Further evidence of this trend is obtained by [Stern \(2015\)](#) (plotted with gray dotted line in Figure 3) using SDSS DR5, tracing at high- $z$  QSOs mainly with  $2 < z < 4$ . They used quadratic function for reproducing the X-ray–MIR luminosity relations.

If the trends above are true, the steeper slope suggests that X-ray emission is inefficient in the high-luminosity end. This is reported by several observations that SED shape of AGN changes with luminosity and Eddington ratio ([Vasudevan & Fabian 2007](#)). The existence of X-



ray weak sources at high bolometric luminosities has been recently confirmed by Ricci et al. (2016a), who found that Hot Dust Obscured Galaxies (hot DOGs; Wu et al. 2012) seem to have X-ray luminosities one or two order of magnitudes below the value expected by the local X-ray – MIR correlation. Since our sample is ultra-hard X-ray selected, our studies might miss those X-ray saturated sources in the high-luminosity end. Those sources could be located faint end in 14–195 keV flux, but not in MIR fluxes. Since BAT 14–195 keV flux limit is over one order of magnitude shallower than those of MIR fluxes, a deeper survey is necessary to assess the luminosity relation between MIR and 14–195 keV luminosity at high luminosity end (see also Figure A1). Another suggestion from this trend is that AGN might have large obscuring fraction in the high luminosity regime and/or in the high- $z$  universe (Buchner et al. 2015). This might be true considering the X-ray studies that the fraction of Compton-thick AGN increase with redshift from  $z = 0$  to  $z = 2$  (Brightman & Ueda 2012). We do not attempt to solve this question at high luminosities here but it is valuable to mention another possibility of the slope differences among those studies of high-luminosity end. One possibility which make the slope steeper originates from the 6  $\mu\text{m}$  bands instead of 12  $\mu\text{m}$ . Asmus et al. (2015) pointed out that hot dust component could dominate around 6  $\mu\text{m}$  (Mor & Netzer 2012) rather than the typical torus warm component which peaks around 20–30  $\mu\text{m}$  (e.g., Mullaney et al. 2011). The contamination from the host galaxies at 6  $\mu\text{m}$  is also possible concern. Mateos et al. (2015) revised the  $L_{6\mu\text{m}}-L_{2-10}$  luminosity relations by using a complete and flux limited sample of  $> 200$  AGN from the Bright Ultra hard *XMM-Newton* Survey and *WISE*. They obtained absorption corrected X-ray luminosities and also derived the 6  $\mu\text{m}$  AGN luminosity by the spectral decomposition of the torus and host galaxies. They applied the Bayesian approach to linear regression with errors in both X and Y-axis by using the IDL command `linmix_err` with the X-ray luminosity as independent variable, which is the same method used by Asmus et al. (2015). They report a slope of  $b = 0.99 \pm 0.03$  (over plotted as green dotted line in Figure 3) up to luminosities of  $L_{2-10} \sim 10^{46} \text{ erg s}^{-1}$ . This agrees well with the results of Asmus et al. (2015) and ours ( $b = 0.96 \pm 0.02$ ). Note that studies by Mateos et al. (2015) also might miss very luminous sources due to the limited survey volume in X-ray, which is possibly making the slope shallower.

Equations (1) and (2) also show that intercept  $a$  of  $L_{22 \mu\text{m}}$  is higher than that of  $L_{12\mu\text{m}}$ . This tendency can be explained by two possibilities, 1) the torus emission peaks in  $\nu F_\nu$  unit at 20–40  $\mu\text{m}$  rather than  $\sim 10 \mu\text{m}$ , which is suggested by both of the observation (Weedman et al. 2005; Buchanan et al. 2006; Mullaney et al. 2011;

Asmus et al. 2011, 2014; Ichikawa et al. 2015; Fuller et al. 2016) and clumpy torus models (Nenkova et al. 2008a; Hönig & Kishimoto 2010; Schartmann et al. 2008). 2) the star formation component contaminates more at longer wavelengths (e.g., Netzer et al. 2007; Mullaney et al. 2011). The former contributes more strongly at high luminosity end ( $L_{14-195} > 10^{44} \text{ erg s}^{-1}$ ) because the relative star formation contamination could be smaller considering the slope of  $L_{\text{FIR}}-L_{14-195}$  is shallower ( $b < 0.94$ ). On the other hand, the latter contributes strongly to lower luminosity sources ( $L_{14-195} < 10^{44} \text{ erg s}^{-1}$ ). This will be discussed again in Section 3.6.

### 3.2. Correlation between the FIR and AGN bolometric luminosities

The correlation between FIR and AGN bolometric luminosity ( $L_{\text{bol}}$ ) could shed the light on the link between the star formation activity of the AGN host galaxies and the accretion rate of AGN. Since the accretion disk emission cannot be directly obtained for all the sources of our sample, the bolometric correction should be applied to  $L_{14-195}$  to estimate the bolometric luminosity. Marconi et al. (2004) account for variations in AGN SEDs by using the well-known anti-correlation between the optical-to-X-ray spectral index ( $\alpha_{\text{OX}}$ ). Then, they renormalize the template SED to a particular  $\alpha_{\text{OX}}$  to obtain the bolometric correction with AGN luminosity. Therefore, they assume a varying relation between optical/UV and X-ray luminosity, not a constant value (e.g., Elvis et al. 1994). A similar approach is followed by Hopkins et al. (2007) who, however used a template SED generated from the averages of real SEDs in different wavebands. There is a systematic difference that the one of Hopkins et al. (2007) is roughly a factor of  $\sim 1.5$  larger than that of Marconi et al. (2004). This is because Hopkins et al. (2007) defines  $L_{\text{bol}}$  as the integral of the observed template SED including the reprocessed emission in the MIR from the accretion disk, whereas Marconi et al. (2004) only integrates the emission of optical-UV and X-ray radiated by the accretion disk itself and hot corona, respectively. Since the accretion rate is better related to the total luminosity directly produced by the accretion process,  $L_{\text{bol}}$  defined by Marconi et al. (2004) is better suited for our study. Hence, we apply the bolometric correction of Marconi et al. (2004) with

$$\log L_{\text{bol}} = 0.0378(\log L_{14-195})^2 - 2.03 \log L_{14-195} + 61.6. \quad (5)$$

Figure 4 shows that FIR luminosities ( $L_{70 \mu\text{m}}, L_{90 \mu\text{m}}$ ) are plotted against  $L_{\text{bol}}$ . The least-squares Bisector fits to the FIR versus bolometric AGN luminosity with a power-law give the correlations of

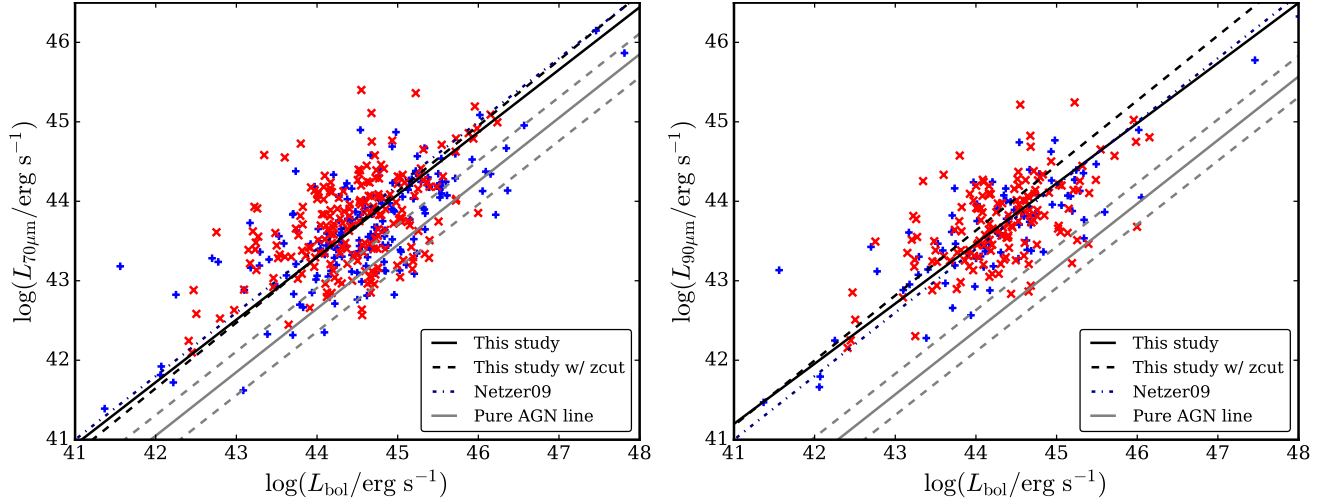


**Figure 4.** Luminosity correlations between the luminosities at 70 and 90  $\mu\text{m}$  ( $L_{70\ \mu\text{m}}, L_{90\ \mu\text{m}}$ ) and bolometric luminosity ( $L_{\text{bol}}$ ) estimated from Equation (5). Blue/red color represents type-1/-2, respectively. The black solid line represents the slope of Equation (6) and (7), respectively. The black dashed line represents the slope of Equation (8) and (9), respectively. The dot-dashed line (navy) represents the slope obtained by Netzer (2009). The gray solid line represents the pure-AGN sequence reported in Equation (11) and (12), respectively.

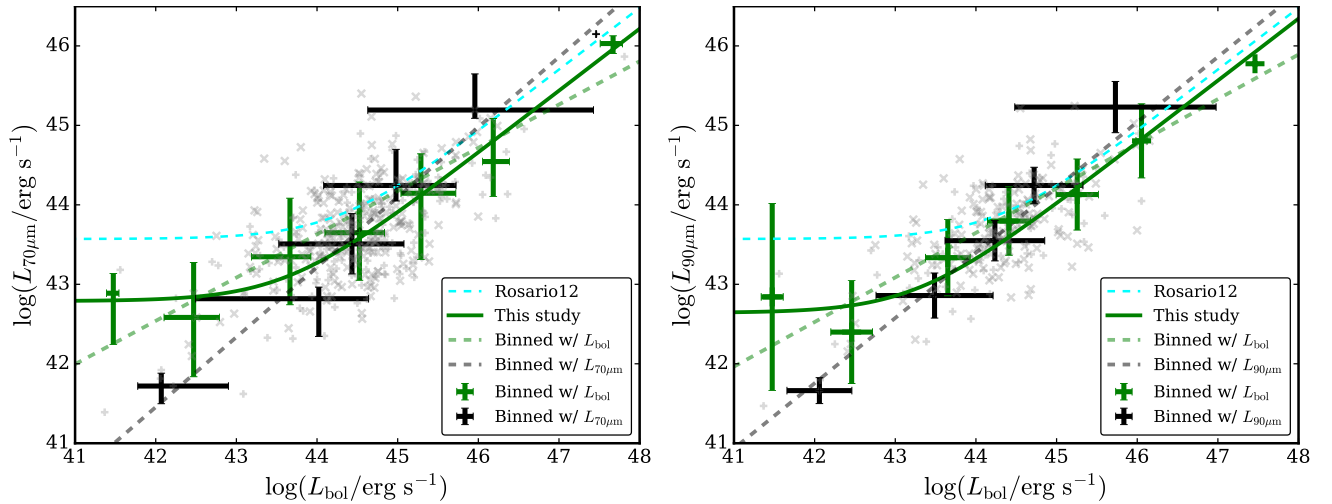


**Figure 5.** Mean luminosity correlations between the luminosities at 70 and 90  $\mu\text{m}$  ( $L_{70\ \mu\text{m}}, L_{90\ \mu\text{m}}$ ) and bolometric luminosity ( $L_{\text{bol}}$ ) estimated from Equation (5). Green color bin represents the mean measurements of 70 and 90  $\mu\text{m}$  luminosity as a function of bolometric luminosity. Black solid bin represents the mean measurements of bolometric luminosity as a function of 70 and 90  $\mu\text{m}$  luminosity, respectively. The gray points represent AGN detected in both bands and are the same data points shown in Figure 4. The green/black dashed line represents the slope obtained by the least-bisector fit for the green/black bin sample, respectively. The cyan dashed line represents the fitted line of local X-ray selected AGN obtained from Rosario et al. (2012). The solid green line represents a fit to the relationship using the same function from as Rosario et al. (2012), but applied to our binned data shown by the green points.

$$\log \frac{L_{70\ \mu\text{m}}}{10^{43}\ \text{erg/s}} = (-0.49 \pm 0.05) + (0.79 \pm 0.03) \log \frac{L_{\text{bol}}}{10^{43}\ \text{erg/s}} \quad (6)$$

$$\log \frac{L_{90\ \mu\text{m}}}{10^{43}\ \text{erg/s}} = (-0.29 \pm 0.05) + (0.76 \pm 0.03) \log \frac{L_{\text{bol}}}{10^{43}\ \text{erg/s}} \quad (7)$$

Since our relations are obtained based on the FIR detected sample, which is not complete (65% for 70  $\mu\text{m}$

band and 45% for 90  $\mu\text{m}$  band) as shown in Figure 1, we check the dependence of the completeness by restricting the redshift down to  $z < 0.076$  for 70  $\mu\text{m}$  and  $z < 0.022$  for 90  $\mu\text{m}$  band to achieve 80% completeness of the IR counterparts, respectively. The relation at each band is given as

$$\log \frac{L_{70\mu\text{m}}}{10^{43} \text{ erg/s}} = (-0.53 \pm 0.06) + (0.83 \pm 0.04) \log \frac{L_{\text{bol}}}{10^{43} \text{ erg/s}} \quad (8)$$

$$\log \frac{L_{90\mu\text{m}}}{10^{43} \text{ erg/s}} = (-0.19 \pm 0.08) + (0.82 \pm 0.05) \log \frac{L_{\text{bol}}}{10^{43} \text{ erg/s}}. \quad (9)$$

The slope here is slightly steeper than those reported in Equation (6) and (7), but the slopes are consistent within the  $1\sigma$  uncertainties (see also Figure 4). Therefore, we conclude that dependence of the completeness is weak.

In addition, we also estimate the effective luminosity range based on the limited volume of the *Swift*/BAT AGN sample. This is because AGN with the highest luminosity are rare and so might be found in the limited *Swift*/BAT survey volume. Likewise, faint AGN will be missing from the sample because of the *Swift*/BAT ultra-hard X-ray flux limits. First, based on the flux limit of *Swift*/BAT survey of  $f_{14-195} = 1.34 \times 10^{-11} \text{ erg s}^{-1} \text{ cm}^{-2}$  (Baumgartner et al. 2013), and the conversion factor of  $f_{2-10} = 2.1 \times f_{14-195}$ , we estimate the survey volume as a function of the flux limited luminosity  $V(L_{2-10}) = (4/3)\pi D_{L_{2-10}}^3 \text{ Mpc}^3$ . Next, we calculate the expected number of AGN detection as a function of  $L_{2-10}$  using the 2-10 keV luminosity function from Ueda et al. (2014) with a  $z$ -dependence of  $\propto (1+z)^4$ . Then, we define the effective luminosity range in which the expected number of detected AGN per dex in  $L_{2-10}$  is greater than 10, which is sufficient to measure the luminosity relation. The result is  $40.8 < \log L_{2-10} < 45.5$  which is equivalent to  $41.1 < \log L_{14-195} < 45.8$  and  $41.8 < \log L_{\text{bol}} < 47.7$ . Therefore, a deeper and/or wider survey is needed to measure the relations between FIR and AGN luminosity both at  $\log L_{\text{bol}} < 41.8$  and  $\log L_{\text{bol}} > 47.7$ .

In Figure 4, we also show the relation of Netzer (2009) (navy dashed line). Our local sample reproduces well the relation of Netzer (2009) using local optical type-2 AGN ( $z \leq 0.2$ ). The difference between our study and that of Netzer (2009) is that while we used  $L_{\text{FIR}}$  as a proxy for star formation, Netzer (2009) used the break at 4000 Å (D4000) for estimating  $L_{\text{FIR}}$ . Matsuoka & Woo (2015) reported that while D4000-based SFR is not well determined at lower SFR since the calibration was based on starburst galaxies, the systematic difference between D4000-based SF luminosity and  $L_{\text{FIR}}$  is small enough compared to the broad distribution between SF luminosity and  $L_{\text{AGN}}$ . Even with the  $L_{\text{FIR}}$ , we find a consistent result with Matsuoka & Woo (2015), using a sample of SDSS DR7 local AGN at  $z < 0.2$ .

Recent studies have reported that “mean” or “binned”  $L_{\text{FIR}}-L_{\text{bol}}$  show a flattened (or even horizontal) pattern in each redshift bin (e.g., Shao et al. 2010; Rosario et al.

2012; Stanley et al. 2015) for  $0 < z < 2.5$ . However, such flattened pattern is not detected in our sample when we use individual luminosity measurements instead of the mean luminosities. To check this, the binned analysis is also applied to our 70  $\mu\text{m}$  or 90  $\mu\text{m}$  detected sources and the results are shown in Figure 5. The plotted bin is the median value in each luminosity bin with errorbars showing the interpercentage range containing 80% of the sample. Green points represent the mean measurements of 70 and 90  $\mu\text{m}$  luminosity averaged in bins of bolometric luminosity, while black points represent the mean bolometric luminosity averaged in bins of 70 and 90  $\mu\text{m}$  luminosity, respectively. The dashed line represents the estimated relation based on the least-square Bisector fits. As shown in the Figure, the slope ( $b = 0.54 \pm 0.08$  for 70  $\mu\text{m}$  and  $b = 0.56 \pm 0.07$  for 90  $\mu\text{m}$ ) of green dashed line (binned with  $L_{\text{bol}}$ ) is significantly shallower than that of the black dashed line (binned with  $L_{\text{FIR}}$ ;  $b = 0.88 \pm 0.05$  for 70  $\mu\text{m}$  and  $b = 0.82 \pm 0.06$  for 90  $\mu\text{m}$ ). To further model the trend of green points, we apply curve fit used in Rosario et al. (2012). The function is written as

$$\log L_{\text{FIR}} = \log (10^{b \log L_{\text{bol}} + \log L_{\text{b}} - b \log L_{\text{c}}} + 10^{\log L_{\text{b}}}) \quad (10)$$

with three free parameters ( $b$ ,  $\log L_{\text{b}}$ ,  $\log L_{\text{c}}$ ) but we fix the slope  $b = 0.78$  by following Rosario et al. (2012).  $L_{\text{b}}$  is a constant value mainly determined by the constant  $L_{\text{FIR}}$  value where  $L_{\text{AGN}}$  is small.  $L_{\text{c}}$  represents the value of  $L_{\text{AGN}}$  where the function becomes equal to  $L_{\text{b}}$ . We fit the green points using a non-linear least squares fitting procedure (curve\_fit in Python). The result is shown with the green solid line in Figure 5. The model nicely reproduces the flattened relation, but systematically smaller value ( $\log L_{\text{b}} = 42.79 \pm 0.02$  for 70  $\mu\text{m}$  and  $\log L_{\text{b}} = 42.64 \pm 0.03$  for 90  $\mu\text{m}$ ) than the line of local AGN ( $\log L_{\text{b}} = 43.57 \pm 0.08$ ) in Rosario et al. (2012). This would be because our sample contains deeper data from *Herschel*, whereas Rosario et al. (2012) use shallower *IRAS*-FSC data for the local AGN and do not apply stacking analysis of non-detection sources for this local sample.

Overall, whereas the IR averaging (in bins of bolometric luminosity, shown by the green points) nicely reproduces the flattened trend as reported in the literature (Shao et al. 2010; Rosario et al. 2012), the black solid bin still holds rising trend almost same as the relation obtained from the individual objects. This could be originated from the different time scale of SF and AGN activity. Hickox et al. (2014) calculated mean  $L_{\text{FIR}}-L_{\text{bol}}$  in two ways. Hickox et al. (2014) constructed a simple model population of SF galaxies in which SF and the BH growth are correlated in galaxies across a range of  $0.25 < z < 1.25$ , with a  $z$  dependent distribution in SFR

from the FIR luminosity function derived by [Gruppioni et al. \(2013\)](#). They assigned an observed average SFR to BH accretion rate of 3000 (e.g., [Rafferty et al. 2011](#); [Mullaney et al. 2012](#); [Chen et al. 2013](#)), and also assumed that the instantaneous accretion rate relative to the average is distributed from the given fiducial luminosity distribution. They first derived the averaged  $L_{\text{bol}}$  for galaxies in each  $L_{\text{FIR}}$  bin and compared the results obtained by [Symeonidis et al. \(2011\)](#) and [Chen et al. \(2013\)](#) for a range of  $0.25 < z < 1.25$ . This reproduces well the rising relation as shown in our study. They next computed the average  $L_{\text{FIR}}$  as a function of  $L_{\text{bol}}$ . This then reproduces well the flattened relation. This result strongly suggests a picture in which SF and BH accretion are closely connected over long timescales, but this correlation is sometimes hidden at low to moderate  $L_{\text{bol}}$  due to the short-term AGN variability. Note that there are clear difference of the sample used in the aforementioned studies and ours. They included all FIR detected galaxies whereas we focused only AGN host galaxies with the both detections in FIR and X-rays. Further studies using the spectral decomposition of IR SEDs will be discussed in a forthcoming paper (K. Ichikawa et al. in prep).

### 3.3. FIR Pure-AGN candidates

If there are luminous AGN hosted by low-SF galaxies, we may find those ‘‘FIR pure-AGN’’ candidates at the bottom right in Figure 4. [Matsuoka & Woo \(2015\)](#) investigated the FIR pure-AGN sequence between  $L_{\text{FIR}}-L_{\text{bol}}$  by adopting a typical AGN SED template of [Mullaney et al. \(2011\)](#). The FIR pure-AGN sequences are given with

$$\log \frac{L_{70 \mu\text{m}}}{\text{erg s}^{-1}} = (7.45 \pm 0.26) + 0.80 \log \frac{L_{\text{bol}}}{\text{erg s}^{-1}} \quad (11)$$

$$\log \frac{L_{90 \mu\text{m}}}{\text{erg s}^{-1}} = (7.17 \pm 0.26) + 0.80 \log \frac{L_{\text{bol}}}{\text{erg s}^{-1}}. \quad (12)$$

In Figure 4, the estimated FIR pure-AGN sequence is also over plotted with gray lines. In this study we define the FIR pure-AGN candidate if the source is located under the FIR pure-AGN sequence in Figure 4. As a result, 50 and 4 sources fulfill the criterion at 70 and 90  $\mu\text{m}$ , respectively. There is a clear number difference between 70 and 90  $\mu\text{m}$  even when we consider the ratio of the FIR pure-AGN to the sample ( $50/388 \sim 13\%$  for 70  $\mu\text{m}$  while  $4/241 \sim 2\%$  for 90  $\mu\text{m}$  criterion). One reason could originate from the sensitivity difference. The sensitivity at 70  $\mu\text{m}$  is better than at 90  $\mu\text{m}$  because of the inclusion of the *Herschel*/PACS detected sources at 70  $\mu\text{m}$ . Of the 50 objects selected at 70  $\mu\text{m}$ , 42 are not detected at 90  $\mu\text{m}$ . It is also likely that, at shorter wavelengths, the typical AGN contribution becomes stronger while the SF contribution becomes weaker (e.g., [Mullaney et al.](#)

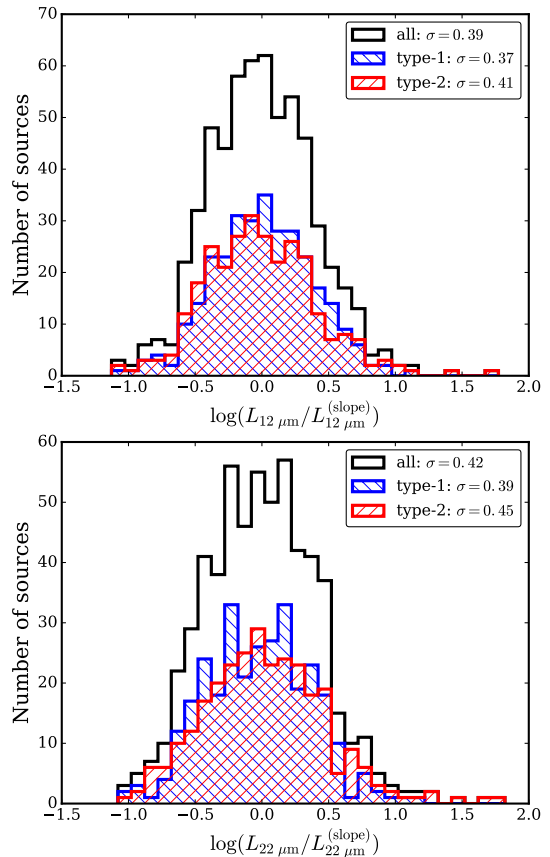


**Figure 6.** Histograms of  $r_{12,22} = \log(L_{12 \mu\text{m},22 \mu\text{m}} / L_{12 \mu\text{m},22 \mu\text{m}}^{(\text{slope})})$  (top and bottom panel, respectively). The solid black/shaded blue/shaded red line represents the total, type-1, and type-2 sample, respectively.

[2011](#)). To support this, all the four pure-AGN candidates at 90  $\mu\text{m}$  also fulfill the criterion at 70  $\mu\text{m}$ , while only 50% (4/8) of 70  $\mu\text{m}$  selected pure-AGN candidates with 90  $\mu\text{m}$  detection fulfill the criterion at 90  $\mu\text{m}$ .

The names of 90  $\mu\text{m}$  selected five sources are NGC 1194, ESO 506-G027, NGC 5252, and CGCG 164-019. All are type-2 AGN and average luminosity is high with  $\langle \log(L_{14-195} / \text{erg s}^{-1}) \rangle = 44.1$ . While those pure-AGN population is quite small with  $\sim 2\%$  (4 out of 274), they are good sample to construct the pure-AGN IR SEDs including the FIR end, and to examine the extrapolation to FIR luminosities from the intrinsic-AGN SED is correct. They also could be in the stage that SF is suppressed because AGN feedback is in action (e.g., [Woo et al. 2016](#)). The future X-ray satellite e-Rosita ([Merloni et al. 2012](#)) will discover over 3-million AGN and cross-matching those with the FIR catalogs would reveal pure-AGN in large numbers.

### 3.4. Distribution of $r_{12,22}$

Figure 6 shows the histograms of the ratio defined as  $r_{12,22} = \log(L_{12 \mu\text{m},22 \mu\text{m}} / L_{12 \mu\text{m},22 \mu\text{m}}^{(\text{slope})})$ , where

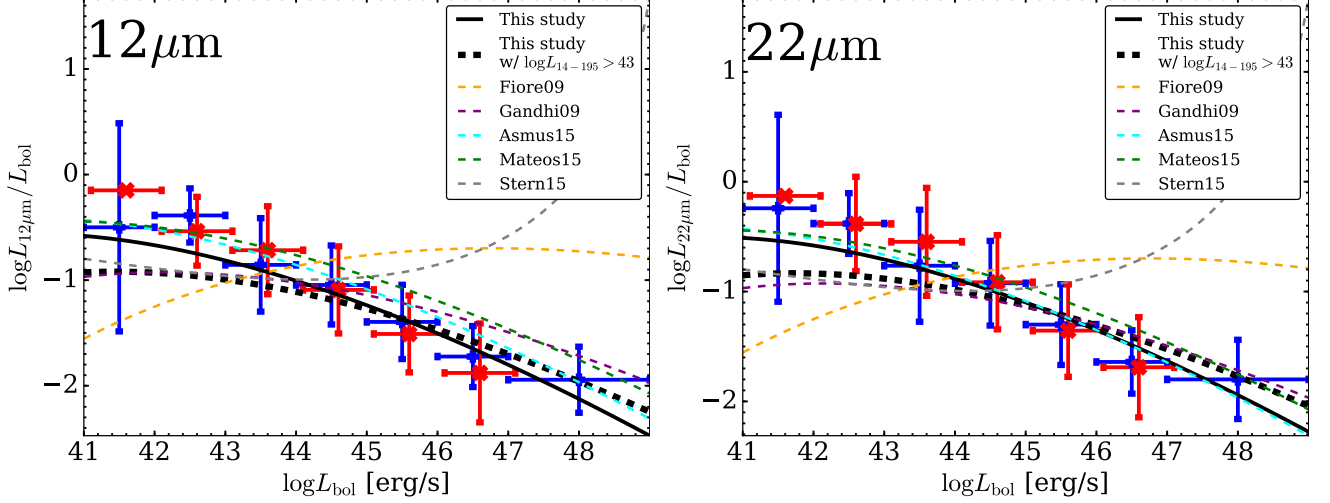


**Figure 7.** MIR luminosity to bolometric luminosity ratio as a function of bolometric luminosity.  $L_{\text{bol}}$  is estimated from Equation 5 for our sample, while from Equation 14 for the other studies from the literature. (Left)  $\log L_{12\mu\text{m}}/L_{\text{bol}}$  versus  $\log L_{\text{bol}}$ . (Right)  $\log L_{22\mu\text{m}}/L_{\text{bol}}$  versus  $\log L_{\text{bol}}$ . Blue cross/red X-shape shows type-1/type-2, respectively. The red crosses are shifted to the right by 0.1 dex for clarity. The main AGN type used in Fiore et al. (2009), Stern (2015) are type-1, and that of Gandhi et al. (2009), Mateos et al. (2015), Asmus et al. (2015), and our study are both of type-1 and type-2 AGN.

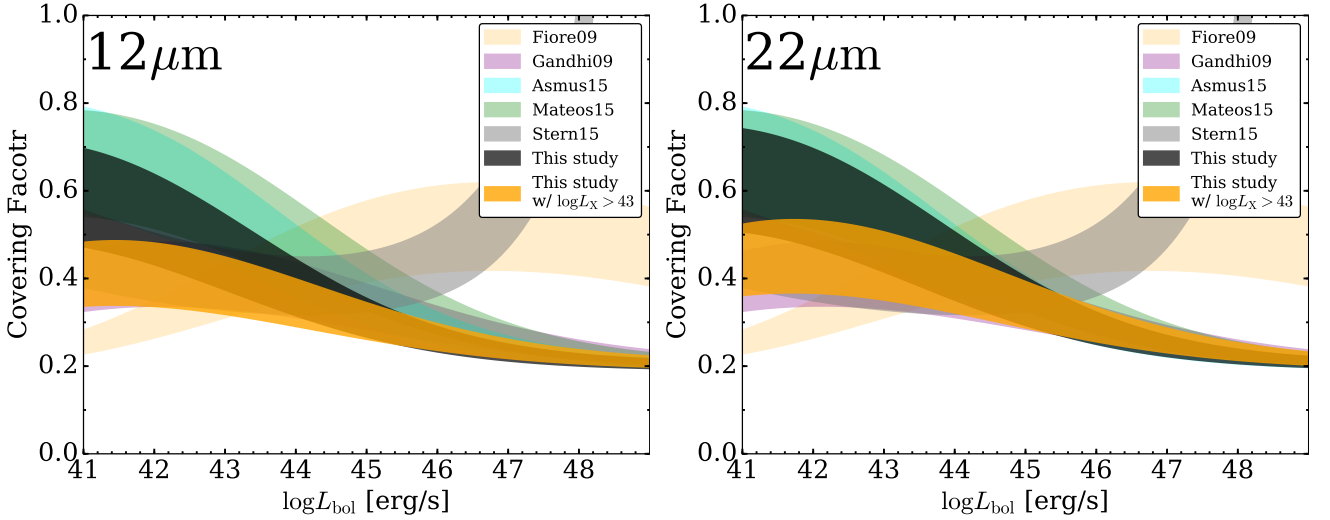


**Figure 8.** Covering factor as a function of bolometric luminosity obtained from 12  $\mu\text{m}$  (left) and 22  $\mu\text{m}$  band (right). The correction from  $L_{\text{MIR}}/L_{\text{bol}}$  is made using the correction function of Stalevski et al. (2016). Each filled area represents the range of the possible covering factor at each  $L_{\text{bol}}$ . Since the corrected function of type-1 AGN always gives the higher value than that of type-2 AGN, we assign an upper limit under the assumption that all sources in this study are type-2 AGN, and a lower limit assuming that all sources are type-1 AGN. The main AGN type used in Fiore et al. (2009), Stern (2015) are type-1, and that of Gandhi et al. (2009), Mateos et al. (2015), Asmus et al. (2015), and our study are both of type-1 and type-2 AGN.

$L_{12\mu\text{m},22\mu\text{m}}^{(\text{slope})}$  represents the expected MIR luminosities obtained from  $L_{14-195}$  using the slopes between  $L_{\text{MIR}}$  and  $L_{14-195}$ . The standard deviation for each sample is compiled in Table 4. The standard deviation for the full sample is  $\sigma = 0.39$  at 12  $\mu\text{m}$  and  $\sigma = 0.42$  at 22  $\mu\text{m}$ . This value is slightly larger than that of Asmus et al. (2015) with  $\sigma = 0.32$ . In 12  $\mu\text{m}$  band, we obtain  $\sigma = 0.40 \pm 0.03$  for type-1 and  $\sigma = 0.43 \pm 0.04$  for type-2 AGN. The scatter is consistent between the type-1 and type-2 AGN in our sample, within the statistical uncer-

tainties, so we find no evidence for a difference in the scatter of the MIR to 14–195 keV X-ray ratio between AGN types. This result might support recent observations that most of the MIR emission comes from the polar extended region with  $\leq 10$  pc scale (e.g., Hönig et al. 2012, 2013; López-Gonzaga et al. 2016) or from even larger  $\simeq 100$  pc scales (Asmus et al. 2016) since an extended geometry of dust more easily produces isotropic MIR emission compared to traditional torus models.

### 3.5. Luminosity Dependence of Covering Factor

We investigate the relation between the AGN and its surrounding dusty torus. Since MIR emission originates from the re-radiation from the dusty torus, one can naturally expect that the ratio of the MIR to AGN luminosity corresponds to the solid angle of the sky covered by the dust (i.e., covering factor;  $C_T$  and  $L_{\text{MIR}} \propto C_T L_{\text{bol}}$ ). Figure 7 shows the luminosity dependence of  $L_{\text{MIR}}/L_{\text{bol}}$ . The black solid and dashed line in Figure 7 represents the estimated line converted from the  $L_{\text{MIR}}-L_{14-195}$  luminosity relations of Equations (1), (2) for the full sample, and Equation (3), (4) for the high-luminosity sample, respectively. We apply Equation 5 for the bolometric correction. Figure 7 shows that  $L_{\text{MIR}}/L_{\text{bol}}$  is declining when  $L_{\text{bol}}$  increases, being consistent with the trend so called “luminosity-dependent unified models”. This model can describe the decrease of covering factor by receding the sublimation radius with the AGN luminosity (Lawrence & Elvis 1982).

However, Lusso et al. (2013) found that corrections for the anisotropy for the dust emission are necessary for using  $L_{\text{MIR}}/L_{\text{bol}}$  as a proxy of the covering factors. In addition, using a 3D Monte Carlo radiation code, Stalevski et al. (2016) reported that the tori of type 1 (viewed from face-on) AGN make  $L_{\text{MIR}}/L_{\text{bol}}$  underestimate low covering factors and overestimate high covering factors. Type 2 (viewed from edge-on) AGN always underestimates covering factors. They also provide the correction functions to account for anisotropy and obtain corrected covering factors. Thus, we derive the corrected covering factor using the combination of the ratio  $L_{12\ \mu\text{m}}/L_{\text{bol}}$ ,  $L_{22\ \mu\text{m}}/L_{\text{bol}}$  and the correction function by Stalevski et al. (2016). We use the correction function of

$$C_T = \begin{cases} -0.178R^4 + 0.875R^3 - 1.487R^2 + 1.408R + 0.192 & (\text{type1}) \\ 2.039R^3 - 3.976R^2 + 2.765R + 0.205 & (\text{type2}) \end{cases} \quad (13)$$

where  $R = L_{\text{MIR}}/L_{\text{bol}}$  and the estimated optical thickness of torus at  $9.7\ \mu\text{m}$  is  $\tau_{9.7} = 3.0$  (see Table 1 of Stalevski et al. (2016) for more details). Figure 8 shows corrected  $C_T$  derived from the slopes tabulated in Table 2 as a function of  $L_{\text{bol}}$  (black solid area). It still holds that  $C_T$  is a declining function of  $L_{\text{bol}}$ , confirming the trend of “luminosity-dependent unified models”.

It is principle possible that the luminosity-dependent trend may be due largely to host galaxy contamination, since the emission from the host galaxy contributes significantly to MIR emission in the low luminosity end as discussed in Section 3.1. To check this effect, in Figures 7 and 8 we also show the  $L_{\text{MIR}}/L_{\text{bol}}$  and the corrected  $C_T$  using the slope with high luminosity sample with  $\log L_{14-195} > 43$ , then extrapolating them to the lower luminosity end. The luminosity dependence of the

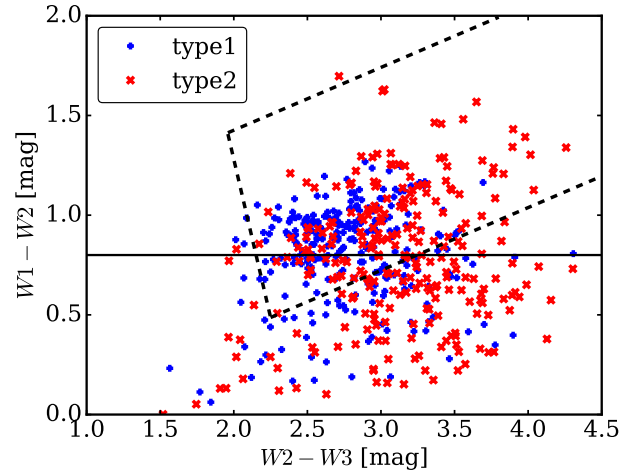


**Figure 9.** W1–W2 versus W2–W3 two color diagram in the unit of Vega magnitude. The two color diagram for each type highlighted with blue (type-1) and red (type-2).

$C_T$  mitigates, but still holds the relations. This idea has been gaining observational evidence from radio (Grimes et al. 2004), IR (Maiolino et al. 2007; Treister et al. 2008; Mor et al. 2009; Alonso-Herrero et al. 2011; Ichikawa et al. 2012b; Toba et al. 2013, 2014), optical (Simpson 2005), and X-ray (Ueda et al. 2003; Beckmann et al. 2009; Ueda et al. 2011; Ricci et al. 2013; Lusso et al. 2013; Ueda et al. 2014) studies of AGN. On the other hand, in the high- $z$  universe with  $z = 2 - 3.5$ , Netzer et al. (2015) reported in their sample infer covering factors consistent with no-evolution with AGN luminosity within the uncertainties for bolometric correction factor.

Again, the previous studies from the literature are also over plotted in Figure 7 and 8 using the bolometric correction of Marconi et al. (2004):

$$\log L_{\text{bol}} = 0.0378(\log L_{2-10})^2 - 2.00 \log L_{2-10} + 60.5 \quad (14)$$

for 2–10 keV luminosity ( $L_{2-10}$ ). As shown in Figure 7 and 8, studies in the local universe (Gandhi et al. 2009; Asmus et al. 2015) found a decrease of the covering factor with the AGN luminosity. Even the high luminosity sample of Mateos et al. (2015) in the high- $z$  universe, same trend can be observed. On the other hand, the studies carried out using high- $L$  (and high- $z$ ) sources by Fiore et al. (2009) and Stern (2015) strongly contradict the luminosity dependent unified models. Considering their rare population of high luminosity AGN in the local universe as discussed in Section 3.2, further investigation with deep survey is necessary for solving this controversy at the high luminosity end.

### 3.6. WISE color-color distribution of Hard X-ray Selected AGN

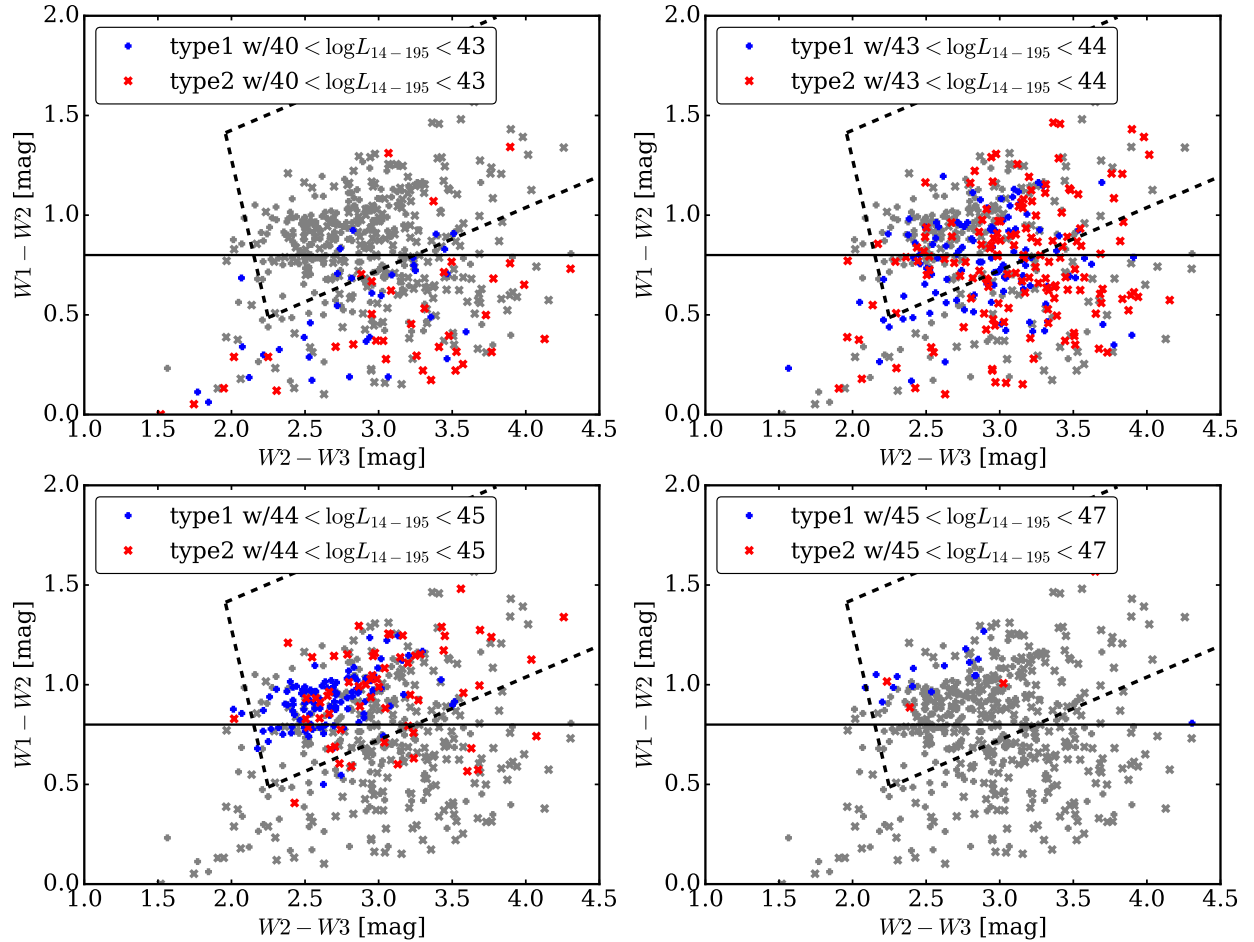


**Figure 10.**  $W1-W2$  versus  $W2-W3$  two color diagram in the unit of Vega magnitude with different BAT luminosity populations, highlighted with blue (type-1) and red (type-2) over plotted with the total sample with gray.

IR color-color selection is useful to identify obscured AGN candidates and also efficient compared to other time-consuming methods such as spectroscopical methods. Figure 9 shows the distribution of AGN on the *WISE* color-color plane. Increasing levels of AGN contribution to the MIR emission have been shown in Figure 10 to move sources upwards in the plane with the color cut  $W1 - W2 = 0.8$  (Stern et al. 2012) and also within the AGN wedge (Mateos et al. 2012). It is clear that our objects do not always locate within the criteria above. As discussed in Section 3.1, lower luminosity sources could have non-negligible level of contamination from the host galaxies in the NIR and MIR bands. To check it quantitatively, we divide the sample into subgroups of luminosities, then calculate the detection rate. Figure 11 shows the detection rate of AGN using the thresholds of Stern et al. (2012) (top) and Mateos et al. (2012) (bottom), respectively. The detection rate increases drastically at  $L_{14-195} > 10^{43}$  erg s $^{-1}$  and most ( $> 80\%$ ) sources can be selected using the IR color-color methods at  $L_{14-195} > 10^{44}$  erg s $^{-1}$ . Thus, while the IR

color-color methods are highly effective at high luminosities ( $L_{14-195} > 10^{44}$  erg s $^{-1}$ ), searching for faint AGN with  $L_{14-195} < 10^{44}$  erg s $^{-1}$  with near IR color-color methods should be complemented with other AGN identification methods such as hard ( $E > 2$  keV) X-rays (e.g., LaMassa et al. 2015).

Figure 11 shows that type-1 and type-2 AGN do not show any significant difference. It indicates that the detection rate does not originate from the different AGN population, such as the effects of the suppressions of NIR SEDs in type-2 AGN due to heavier obscuration by the torus clumps (Ramos Almeida et al. 2011), but more likely by the dilution from the host galaxy stellar direct emission which causes blue  $W1 - W2$  colors (e.g., Stern et al. 2005; Risaliti et al. 2006; Sani et al. 2008; Imanishi et al. 2010; Ichikawa et al. 2014). The same trend is also reported in Toba et al. (2014), which used the *WISE*-matched SDSS AGN selected by the BPT diagram (Baldwin et al. 1981). They showed that *WISE* color-method efficiency increases with  $L_{22 \mu\text{m}}$ . Kawamuro et al. (2016b) also reported that hard X-ray se-

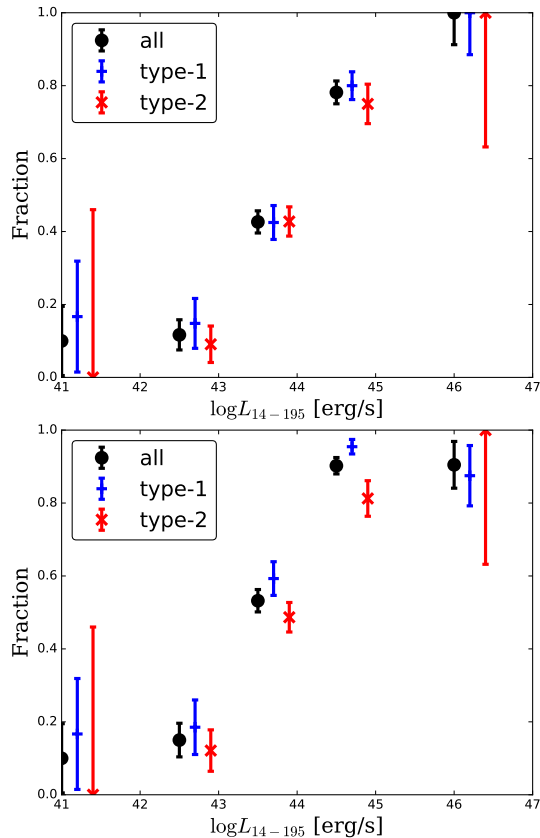


**Figure 11.** Fraction of AGN that meet the IR color selections as a function of BAT luminosity (in logarithmic units) highlighted with black filled circle (all), blue cross (type-1), and red cross (type-2) color. (Top) color cut with  $W1 - W2 > 0.8$  by Stern et al. (2012). (Bottom) color cut by Mateos et al. (2012).

lected low-luminosity AGN cannot be found using the IR color selections above. These results are consistent with what is shown in Figure 11 by considering that most sources are at  $L_{14-195} < 10^{44}$  erg s $^{-1}$ . The same trend is also reported from the X-ray studies of Compton-thick AGN (Gandhi et al. 2015; Tanimoto et al. 2016). They reported that secure Compton-thick AGN in the local universe do not preferentially locate within the AGN cut or wedge at  $L_{14-195} < 10^{43}$  erg s $^{-1}$ . However, even for the luminous AGN, if they are heavily obscured AGN such as buried AGN, NIR and even MIR absorption may play a role to locate them outside the AGN cut or wedge (e.g., Hainline et al. 2014b; Imanishi et al. 2016). In addition, some authors (e.g., Satyapal et al. 2014; Secrest et al. 2015) find that the fraction of AGN by *WISE* color selection is highest at lower stellar masses and drops dramatically in higher mass galaxies, suggesting the stellar mass (or, Eddington-ratio) is another key parameter affecting the success rate of the IR color selections as well as the X-ray luminosity discussed above.

#### 4. CONCLUSIONS

We have compiled the IR (3–500  $\mu$ m) counterparts of a nearby complete flux limited 604 AGN sources detected in the 70-month integration of the *Swift*/BAT all-sky survey in the 14–195 keV band. Utilizing the IR catalogs obtained from *WISE*, *AKARI*, *IRAS*, and *Herschel*, we identified 604, 560, 601, and 402 counterpart in the any IR, NIR, MIR, and FIR band, respectively. For our discussion, the detected sources are divided into two AGN types based on  $N_{\text{H}}$  with a boundary of  $N_{\text{H}} = 10^{22}$  cm $^{-2}$ . Our results are summarized as follows:

1. We find a good luminosity correlation between the MIR and ultra hard X-ray band over 5 orders of magnitude ( $41 < \log(L_{14-195}/\text{erg s}^{-1}) < 46$ ). Using the linear relation of  $\log(L_{\text{MIR}}/10^{43} \text{ erg s}^{-1}) = a + b \log(L_{14-195}/10^{43} \text{ erg s}^{-1})$ , the slope  $b = 0.96 - 0.98$  is obtained for the whole sample and  $b = 1.05 - 1.07$  for the high luminosity sample ( $L_{14-195} > 10^{43}$  erg s $^{-1}$ ). This value is consistent with those obtained by high spatial resolution MIR image observations of X-ray selected catalogs. Whereas the slope is shallower than that obtained from the sample of high- $z$  optically selected luminous AGN. This indicates that X-ray emission could be saturated than MIR ones in the high-luminosity end.
2. We find a rising trend between bolometric AGN power and FIR over 5 orders of magnitude in the individual plots. The slope is consistent with that obtained by Netzer (2009) as well as Matsuoka & Woo (2015). The binned analysis also shows that mean  $L_{\text{bol}}$  as a function of  $L_{\text{FIR}}$  shows the rising trend, which is consistent with the individual plot analysis. However, the mean  $L_{\text{FIR}}$  as a function of  $L_{\text{bol}}$  shows a flattened trend. This seemingly contradicting result could be originated from the difference of the dominant timescale between SF and AGN activity that SF and BH accretion is closely connected over long timescales, but this relation can be hidden at lower  $L_{\text{bol}}$  due to the short-term AGN variability (e.g., Mullaney et al. 2012; Chen et al. 2013; Hickox et al. 2014)
3. We find a small number of FIR pure-AGN candidates which have strong AGN luminosity with very weak SF contribution from their host galaxies. These objects represent a good sample to construct the pure-AGN IR SED including the FIR end. They could be good candidates to study AGN feedback since they might be in the stage that SF activity is suppressed due to energy output from the AGN.
4. Using the correction from MIR to bolometric luminosity ratio to covering factor by Stalevski



*et al.* (2016), we find the covering factor decreases with bolometric luminosities, confirming the luminosity-dependent unified model.

5. We find that the efficiency of the *WISE* color cuts proposed by Stern *et al.* (2012) and Mateos *et al.* (2012) is highly AGN luminosity dependent. These methods cannot completely pick up local X-ray selected low-luminosity AGN with  $L_{14-195} < 10^{44}$  erg s $^{-1}$ , while the color-color cut methods efficiently pick up most AGN with  $L_{14-195} > 10^{44}$  erg s $^{-1}$ .

We thank the anonymous referee for a very careful reading of the manuscript and numerous helpful suggestions that greatly strengthened the paper. This re-

search has made use of the NASA/IPAC Extragalactic Database (NED) which is operated by the Jet Propulsion Laboratory, California Institute of Technology, under contract with the National Aeronautics and Space Administration. This research has made use of “Aladin sky atlas” developed at CDS, Strasbourg Observatory, France (Bonnarel *et al.* 2000; Boch & Fernique 2014). K.I. thanks the Department of Astronomy at Kyoto university, where a part of the research was conducted. K.I. and Y.U. acknowledge support from JSPS Grant-in-Aid for Scientific Research (grant number 40756293: KI, 26400228: YU). C.R. acknowledge financial support from the CONICYT-Chile grants “EM-BIGGEN” Anillo ACT1101, FONDECYT 1141218, and Basal-CATA PFB-06/2007. Part of this was financially supported by the Grant-in-Aid for JSPS fellow for young researchers (PD; KI. KM; DC1; TK.).

## REFERENCES

- Alonso-Herrero, A., Ramos Almeida, C., Mason, R., *et al.* 2011, *ApJ*, 736, 82
- Asmus, D., Gandhi, P., Smette, A., Hönig, S. F., & Duschl, W. J. 2011, *A&A*, 536, A36
- Asmus, D., Hönig, S. F., Gandhi, P., Smette, A., & Duschl, W. J. 2014, *MNRAS*, 439, 1648
- Asmus, D., Gandhi, P., Hönig, S. F., Smette, A., & Duschl, W. J. 2015, *MNRAS*, 454, 766
- Asmus, D., Hönig, S. F., & Gandhi, P. 2016, *ApJ*, 822, 109
- Assef, R. J., Stern, D., Kochanek, C. S., *et al.* 2013, *ApJ*, 772, 26
- Baldwin, J. A., Phillips, M. M., & Terlevich, R. 1981, *PASP*, 93, 5
- Barthelmy, S. D., Barbier, L. M., Cummings, J. R., *et al.* 2005, *SSRv*, 120, 143
- Baumgartner, W. H., Tueller, J., Markwardt, C. B., *et al.* 2013, *ApJS*, 207, 19
- Beckmann, V., Soldi, S., Ricci, C., *et al.* 2009, *A&A*, 505, 417
- Beichman, C. A., Neugebauer, G., Habing, H. J., Clegg, P. E., & Chester, T. J. 1988, *Infrared astronomical satellite (IRAS) catalogs and atlases. Volume 1: Explanatory supplement*, 1
- Berney, S., Koss, M., Trakhtenbrot, B., *et al.* 2015, *MNRAS*, 454, 3622
- Boch, T., & Fernique, P. 2014, *Astronomical Data Analysis Software and Systems XXIII*, 485, 277
- Bonnarel, F., Fernique, P., Bienaymé, O., *et al.* 2000, *A&AS*, 143, 33
- Brightman, M., & Ueda, Y. 2012, *MNRAS*, 423, 702
- Buchanan, C. L., Gallimore, J. F., O’Dea, C. P., *et al.* 2006, *AJ*, 132, 401
- Buchner, J., Georgakakis, A., Nandra, K., *et al.* 2015, *ApJ*, 802, 89
- Burlon, D., Ajello, M., Greiner, J., *et al.* 2011, *ApJ*, 728, 58
- Castro, A., Miyaji, T., Shirahata, M., *et al.* 2014, [arXiv:1408.3172](https://arxiv.org/abs/1408.3172)
- Chen, C.-T. J., Hickox, R. C., Alberts, S., *et al.* 2013, *ApJ*, 773, 3
- Chen, C.-T. J., Hickox, R. C., Alberts, S., *et al.* 2015, *ApJ*, 802, 50
- Cutri, R. M., Wright, E. L., Conrow, T., *et al.* 2013, *Explanatory Supplement to the AllWISE Data Release Products*, by R. M. Cutri *et al.*, 1
- Di Matteo, T., Springel, V., & Hernquist, L. 2005, *Nature*, 433, 604
- Donley, J. L., Koekemoer, A. M., Brusa, M., *et al.* 2012, *ApJ*, 748, 142
- Efstathiou, A., & Rowan-Robinson, M. 1995, *MNRAS*, 273, 649
- Eguchi, S., Ueda, Y., Terashima, Y., Mushotzky, R., & Tueller, J. 2009, *ApJ*, 696, 1657
- Eguchi, S., Ueda, Y., Awaki, H., *et al.* 2011, *ApJ*, 729, 31
- Elitzur, M., Ho, L. C., & Trump, J. R. 2014, *MNRAS*, 438, 3340
- Elvis, M., Maccacaro, T., Wilson, A. S., *et al.* 1978, *MNRAS*, 183, 129
- Elvis, M., Wilkes, B. J., McDowell, J. C., *et al.* 1994, *ApJS*, 95, 1
- Fiore, F., Puccetti, S., Brusa, M., *et al.* 2009, *ApJ*, 693, 447
- Fuller, L., Lopez-Rodriguez, E., Packham, C., *et al.* 2016, *MNRAS*, 462, 2618
- Gandhi, P., Horst, H., Smette, A., *et al.* 2009, *A&A*, 502, 457
- Gandhi, P., Lansbury, G. B., Alexander, D. M., *et al.* 2014, *ApJ*, 792, 117
- Gandhi, P., Yamada, S., Ricci, C., *et al.* 2015, *MNRAS*, 449, 1845
- García-Berete, I., *et al.* 2016, *MNRAS* in press. [arXiv:1608.06513](https://arxiv.org/abs/1608.06513)
- García-González, J., Alonso-Herrero, A., Hernán-Caballero, A., *et al.* 2016, *MNRAS*, 458, 4512
- González-Martín, O., Masegosa, J., Márquez, I., Guerrero, M. A., & Dultzin-Hacyan, D. 2006, *A&A*, 460, 45
- González-Martín, O., Masegosa, J., Márquez, I., Guainazzi, M., & Jiménez-Bailón, E. 2009, *A&A*, 506, 1107
- Goulding, A. D., Forman, W. R., Hickox, R. C., *et al.* 2014, *ApJ*, 783, 40
- Griffin, M. J., Abergel, A., Abreu, A., *et al.* 2010, *A&A*, 518, L3
- Grimes, J. A., Rawlings, S., & Willott, C. J. 2004, *MNRAS*, 349, 503
- Gruppioni, C., Pozzi, F., Rodighiero, G., *et al.* 2013, *MNRAS*, 432, 23
- Hainline, K. N., Hickox, R., Greene, J. E., Myers, A. D., & Zakamska, N. L. 2013, *ApJ*, 774, 145
- Hainline, K. N., Hickox, R. C., Greene, J. E., *et al.* 2014, *ApJ*, 787, 65
- Hainline, K. N., Hickox, R. C., Carroll, C. M., *et al.* 2014, *ApJ*, 795, 124
- Hao, L., Weedman, D. W., Spoon, H. W. W., *et al.* 2007, *ApJL*, 655, L77
- Harrison, F. A., Craig, W. W., Christensen, F. E., *et al.* 2013, *ApJ*, 770, 103

- Hatziminaoglou, E., Omont, A., Stevens, J. A., et al. 2010, *A&A*, 518, L33
- Hickox, R. C., Jones, C., Forman, W. R., et al. 2007, *ApJ*, 671, 1365
- Hickox, R. C., Jones, C., Forman, W. R., et al. 2009, *ApJ*, 696, 891
- Hickox, R. C., Mullaney, J. R., Alexander, D. M., et al. 2014, *ApJ*, 782, 9
- Ho, L. C. 2008, *ARA&A*, 46, 475
- Hönig, S. F., Beckert, T., Ohnaka, K., & Weigelt, G. 2006, *A&A*, 452, 459
- Hönig, S. F., & Kishimoto, M. 2010, *A&A*, 523, A27
- Hönig, S. F., Leipski, C., Antonucci, R., & Haas, M. 2011, *ApJ*, 736, 26
- Hönig, S. F., Kishimoto, M., Antonucci, R., et al. 2012, *ApJ*, 755, 149
- Hönig, S. F., Kishimoto, M., Tristram, K. R. W., et al. 2013, *ApJ*, 771, 87
- Hopkins, P. F., Richards, G. T., & Hernquist, L. 2007, *ApJ*, 654, 731
- Hopkins, P. F., Hernquist, L., Cox, T. J., & Kereš, D. 2008, *ApJS*, 175, 356-389
- Horst, H., Smette, A., Gandhi, P., & Duschl, W. J. 2006, *A&A*, 457, L17
- Ichikawa, K., Ueda, Y., Terashima, Y., et al. 2012a, *ApJ*, 754, 45
- Ichikawa, K., Ueda, Y., Terashima, Y., et al. 2012b, *Torus Workshop*, 2012, 109
- Ichikawa, K., Imanishi, M., Ueda, Y., et al. 2014, *ApJ*, 794, 139
- Ichikawa, K., Packham, C., Ramos Almeida, C., et al. 2015, *ApJ*, 803, 57
- Ichikawa, K., Ueda, J., Shidatsu, M., Kawamuro, T., & Matsuoka, K. 2016, *PASJ*, 68, 9
- Imanishi, M., Nakagawa, T., Shirahata, M., Ohyama, Y., & Onaka, T. 2010, *ApJ*, 721, 1233
- Imanishi, M., Imase, K., Oi, N., & Ichikawa, K. 2011, *AJ*, 141, 156
- Imanishi, M., Nakanishi, K., and Izumi, T., *AJ* in press, arXiv:1609.01291
- Isobe, T., Feigelson, E. D., Akritas, M. G., & Babu, G. J. 1990, *ApJ*, 364, 104
- Kawada, M., Baba, H., Barthel, P. D., et al. 2007, *PASJ*, 59, 389
- Kawaguchi, T., & Mori, M. 2010, *ApJL*, 724, L183
- Kawaguchi, T., & Mori, M. 2011, *ApJ*, 737, 105
- Kawamuro, T., Ueda, Y., Tazaki, F., & Terashima, Y. 2013, *ApJ*, 770, 157
- Kawamuro, T., et al. 2016, *ApJ* in press, arXiv:1604.07915
- Kawamuro, T., Ueda, Y., Tazaki, F., Ricci, C., & Terashima, Y. 2016, *ApJS*, 225, 14
- Koss, M., et al. 2016, *ApJ*, submitted
- Krabbe, A., Böker, T., & Maiolino, R. 2001, *ApJ*, 557, 626
- Krolik, J. H., & Begelman, M. C. 1986, *ApJL*, 308, L55
- Lacy, M., Storrie-Lombardi, L. J., Sajina, A., et al. 2004, *ApJS*, 154, 166
- LaMassa, S. M., Civano, F., Brusa, M., et al. 2015, arXiv:1511.02883
- Lawrence, A., & Elvis, M. 1982, *ApJ*, 256, 410
- Levenson, N. A., Radomski, J. T., Packham, C., et al. 2009, *ApJ*, 703, 390
- López-Gonzaga, N., Burtscher, L., Tristram, K. R. W., Meisenheimer, K., & Schartmann, M. 2016, *A&A*, 591, A47
- Lusso, E., Hennawi, J. F., Comastri, A., et al. 2013, *ApJ*, 777, 86
- Lutz, D., Maiolino, R., Spoon, H. W. W., & Moorwood, A. F. M. 2004, *A&A*, 418, 46
- Maiolino, R., Shemmer, O., Imanishi, M., et al. 2007, *A&A*, 468, 979
- Marconi, A., Risaliti, G., Gilli, R., et al. 2004, *MNRAS*, 351, 169
- Massaro, E., Maselli, A., Leto, C., et al. 2015, *Ap&SS*, 357, 75
- Mateos, S., Alonso-Herrero, A., Carrera, F. J., et al. 2012, *MNRAS*, 426, 3271
- Mateos, S., Carrera, F. J., Alonso-Herrero, A., et al. 2015, *MNRAS*, 449, 1422
- Matsuoka, K., & Woo, J.-H. 2015, *ApJ*, 807, 28
- Matsuta, K., Gandhi, P., Dotani, T., et al. 2012, *ApJ*, 753, 104
- Meléndez, M., Mushotzky, R. F., Shimizu, T. T., Barger, A. J., & Cowie, L. L. 2014, *ApJ*, 794, 152
- Merloni, A., Predehl, P., Becker, W., et al. 2012, arXiv:1209.3114
- Merloni, A., Bongiorno, A., Brusa, M., et al. 2014, *MNRAS*, 437, 3550
- Miyaji, T., Hasinger, G., Salvato, M., et al. 2015, *ApJ*, 804, 104
- Mor, R., Netzer, H., & Elitzur, M. 2009, *ApJ*, 705, 298
- Mor, R., & Netzer, H. 2012, *MNRAS*, 420, 526
- Mullaney, J. R., Alexander, D. M., Goulding, A. D., & Hickox, R. C. 2011, *MNRAS*, 414, 1082
- Mullaney, J. R., Daddi, E., Béthermin, M., et al. 2012, *ApJL*, 753, L30
- Mushotzky, R. F., Shimizu, T. T., Meléndez, M., & Koss, M. 2014, *ApJL*, 781, L34
- Nenkova, M., Ivezić, Ž., & Elitzur, M. 2002, *ApJL*, 570, L9
- Nenkova, M., Sirocky, M. M., Ivezić, Ž., & Elitzur, M. 2008, *ApJ*, 685, 147
- Nenkova, M., Sirocky, M. M., Nikutta, R., Ivezić, Ž., & Elitzur, M. 2008, *ApJ*, 685, 160
- Netzer, H., Lira, P., Trakhtenbrot, B., Shemmer, O., & Cury, I. 2007, *ApJ*, 671, 1256
- Netzer, H. 2009, *MNRAS*, 399, 1907
- Netzer, H., Lani, C., Nordon, R., et al. 2015, arXiv:1511.07876
- Oh, K., Schawinski, K., Koss, M., et al. 2016, arXiv:1609.08625
- Onaka, T., Matsuohara, H., Wada, T., et al. 2007, *PASJ*, 59, 401
- Pier, E. A., & Krolik, J. H. 1992, *ApJ*, 401, 99
- Pier, E. A., & Krolik, J. H. 1993, *ApJ*, 418, 673
- Poglitich, A., Waelkens, C., Geis, N., et al. 2010, *A&A*, 518, L2
- Rafferty, D. A., Brandt, W. N., Alexander, D. M., et al. 2011, *ApJ*, 742, 3
- Ramos Almeida, C., Pérez García, A. M., Acosta-Pulido, J. A., & Rodríguez Espinosa, J. M. 2007, *AJ*, 134, 2006
- Ramos Almeida, C., Levenson, N. A., Alonso-Herrero, A., et al. 2011, *ApJ*, 731, 92
- Ramos Almeida, C., Alonso-Herrero, A., Levenson, N. A., et al. 2014, *MNRAS*, 439, 3847
- Ricci, C., Walter, R., Courvoisier, T. J.-L., & Paltani, S. 2011, *A&A*, 532, A102
- Ricci, C., Paltani, S., Awaki, H., et al. 2013, *A&A*, 553, A29
- Ricci, C., Ueda, Y., Paltani, S., et al. 2014, *MNRAS*, 441, 3622
- Ricci, C., Ueda, Y., Koss, M. J., et al. 2015, *ApJL*, 815, L13
- Ricci, C., Assef, R. J., Stern, D., et al. 2016, *ApJin press.*, arXiv:1609.04808
- Ricci, C., et al. 2016, *ApJ*, submitted
- Risaliti, G., Maiolino, R., Marconi, A., et al. 2006, *MNRAS*, 365, 303
- Rodríguez Espinosa, J. M., Rudy, R. J., & Jones, B. 1987, *ApJ*, 312, 555
- Rosario, D. J., Santini, P., Lutz, D., et al. 2012, *A&A*, 545, A45
- Rovilo, E., Comastri, A., Gilli, R., et al. 2012, *A&A*, 546, A58
- Sanders, D. B., Soifer, B. T., Elias, J. H., et al. 1988, *ApJ*, 325, 74
- Sani, E., Risaliti, G., Salvati, M., et al. 2008, *ApJ*, 675, 96
- Satyapal, S., Secrest, N. J., McAlpine, W., et al. 2014, *ApJ*, 784, 113
- Sazonov, S., Willner, S. P., Goulding, A. D., et al. 2012, *ApJ*, 757, 181
- Schartmann, M., Meisenheimer, K., Camenzind, M., et al. 2008, *A&A*, 482, 67
- Secrest, N. J., Dudik, R. P., Dorland, B. N., et al. 2015, *ApJS*, 221, 12

- Shao, L., Lutz, D., Nordon, R., et al. 2010, *A&A*, 518, L26
- Shimizu, T. T., Meléndez, M., Mushotzky, R. F., et al. 2016, *MNRAS*, 456, 3335
- Siebenmorgen, R., Heymann, F., & Efstathiou, A. 2015, *A&A*, 583, A120
- Simpson, C. 1998, *ApJ*, 509, 653
- Simpson, C. 2005, *MNRAS*, 360, 565
- Stalevski, M., Fritz, J., Baes, M., Nakos, T., Popovic, L. 2012, *MNRAS*, 240, 2756
- Stalevski, M., Ricci, C., Ueda, Y., et al. 2016, *MNRAS*, accepted
- Stanley, F., Harrison, C. M., Alexander, D. M., et al. 2015, *MNRAS*, 453, 591
- Stern, D., Eisenhardt, P., Gorjian, V., et al. 2005, *ApJ*, 631, 163
- Stern, D., Assef, R. J., Benford, D. J., et al. 2012, *ApJ*, 753, 30
- Stern, D. 2015, *ApJ*, 807, 129
- Symeonidis, M., Georgakakis, A., Seymour, N., et al. 2011, *MNRAS*, 417, 2239
- Tanimoto, A., Ueda, Y., Kawamuro, T., & Ricci, C. 2016, *arXiv:1601.05056*
- Toba, Y., Oyabu, S., Matsuhara, H., et al. 2013, *PASJ*, 65,
- Toba, Y., Oyabu, S., Matsuhara, H., et al. 2014, *ApJ*, 788, 45
- Treister, E., Krolik, J. H., & Dullemond, C. 2008, *ApJ*, 679, 140
- Ueda, Y., Akiyama, M., Ohta, K., & Miyaji, T. 2003, *ApJ*, 598, 886
- Ueda, Y., Eguchi, S., Terashima, Y., et al. 2007, *ApJL*, 664, L79
- Ueda, Y., Hiroi, K., Isobe, N., et al. 2011, *PASJ*, 63, S937
- Ueda, Y., Akiyama, M., Hasinger, G., Miyaji, T., & Watson, M. G. 2014, *ApJ*, 786, 104
- Ueda, Y., Hashimoto, Y., Ichikawa, K., et al. 2015, *ApJ*, 815, 1
- Vasudevan, R. V., & Fabian, A. C. 2007, *MNRAS*, 381, 1235
- Weedman, D. W., Hao, L., Higdon, S. J. U., et al. 2005, *ApJ*, 633, 706
- Winkler, C., Courvoisier, T. J.-L., Di Cocco, G., et al. 2003, *A&A*, 411, L1
- Winter, L. M., Mushotzky, R. F., Reynolds, C. S., & Tueller, J. 2009, *ApJ*, 690, 1322
- Woo, J.-H., Bae, H.-J., Son, D., & Karouzos, M. 2016, *ApJ*, 817, 108
- Wu, J., Tsai, C.-W., Sayers, J., et al. 2012, *ApJ*, 756, 96
- Wright, E. L., Eisenhardt, P. R. M., Mainzer, A. K., et al. 2010, *AJ*, 140, 1868

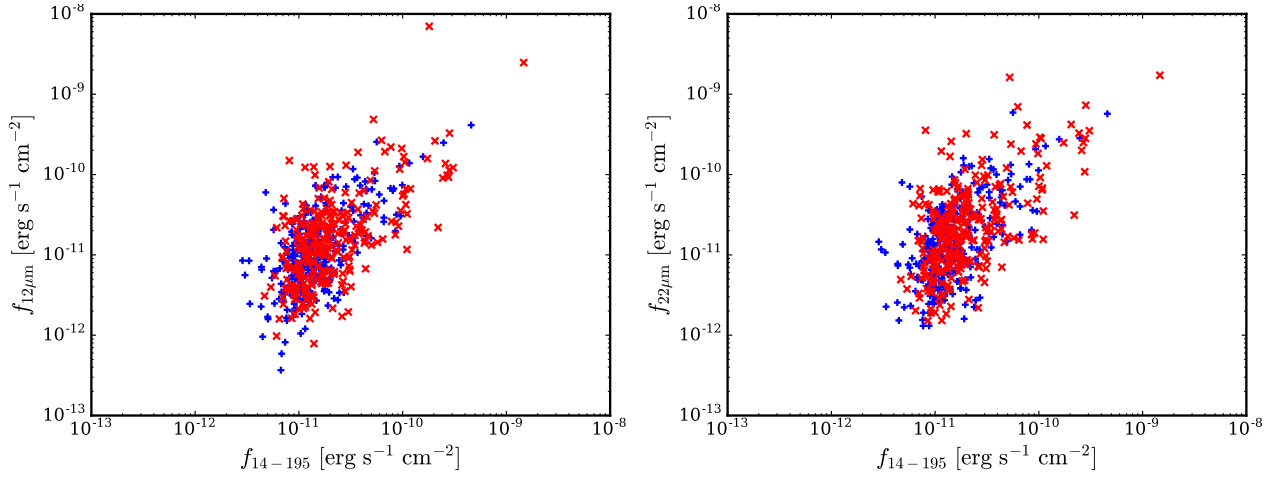


**Figure A1.** Correlation between the fluxes at each MIR band and  $L_{14-195 \text{ keV}}$  for the 12 and 22  $\mu\text{m}$  band. Blue/red color represents type-1/-2, respectively.

## APPENDIX

### A. FLUX CORRELATION BETWEEN MIR BANDS AND 14–195 KEV

Figure A1 shows the flux correlations between the MIR (12 and 22  $\mu\text{m}$ ) and 14–195 keV. This shows that there is a clear correlation between two bands even in the flux-flux plots. The figure also clearly shows that our sample is X-ray flux limited. There is a clear sharp decline of the number of AGN in the sample at faint 14–195 keV fluxes, especially at  $f_{14-195} < 10^{-11} \text{ erg s}^{-1} \text{ cm}^{-2}$ . The MIR detection limits for these sources are typically  $2.5 \times 10^{-13} \text{ erg s}^{-1} \text{ cm}^{-2}$  in the 12  $\mu\text{m}$  and  $8.1 \times 10^{-13} \text{ erg s}^{-1} \text{ cm}^{-2}$  in the 22  $\mu\text{m}$ , which are below the detected fluxes from the sources. Therefore the sample is effectively complete in the MIR and the selection is dominated by the X-ray flux limits as discussed in Section 3.1.

Table 1. IR and 14–195 keV X-ray Properties of the *Swift*/BAT 70-Month AGN Catalog

(1)	(2)	(3)	(4)	(5)	(6)	(7)	(8)	(9)	(10)	(11)	(12)	(13)	(14)	(15)	(16)	(17)	(18)	(19)	(20)	(21)	(22)	(23)	(24)	(25)	(26)	(27)	(28)
No.	Name	$z$	$f_{3.4}$	$f_{4.6}$	$f_{12}$	$f_{22}$	$f_{70}$	$f_{90}$	$f_{140}$	$f_{160}$	$f_{250}$	$f_{350}$	$f_{500}$	IR Catalog	$L_{3.4}$	$L_{4.6}$	$L_{12}$	$L_{22}$	$L_{70}$	$L_{90}$	$L_{140}$	$L_{160}$	$L_{250}$	$L_{350}$	$L_{500}$	$C_{T,12}$	$C_{T,22}$
2	Fairall 1203	0.058400	...	...	...	...	0.196	...	...	...	...	...	...	(X,X,If,X,X)	...	...	...	...	43.87	...	...	...	...	...	...	...	...
3	NGC 7811	0.025500	0.015	0.015	0.052	0.103	0.456	...	...	...	...	...	...	(W,W,If,X,X)	43.31	43.17	43.28	43.32	43.50	...	...	...	...	...	...	0.404	0.418
6	Mrk 335	0.025800	0.072	0.099	0.163	0.312	0.309	...	0.150	0.068	...	...	...	(W,W,H,X,H)	43.98	43.99	43.79	43.81	43.30	...	...	42.63	42.09	...	...	0.507	0.515
7	2MASX J00091156-0036551	0.073300	0.005	0.008	...	...	...	...	...	...	...	...	...	(X,X,X,X,X)	43.80	43.85	...	...	...	...	...	...	...	...	...	...	...
10	2MASX J00210753-1910056	0.095600	0.011	0.013	0.023	0.054	...	...	...	...	...	...	...	(W,W,X,X,X)	44.35	44.30	44.12	44.23	...	...	...	...	...	...	...	0.222	0.230
14	2MASX J00264073-5309479	0.062900	0.009	0.009	0.013	0.024	...	...	...	...	...	...	...	(W,W,X,X,X)	43.89	43.77	43.49	43.50	...	...	...	...	...	...	...	0.218	0.218
16	[HB89] 0026+129	0.14200	0.013	0.017	0.028	0.048	...	...	...	...	...	...	...	(W,W,X,X,X)	44.78	44.78	44.58	44.55	...	...	...	...	...	...	...	0.228	0.226
17	ESO112-6	0.029000	0.010	0.007	0.025	0.049	1.019	1.183	...	...	...	...	...	(W,W,Ip,A,X)	43.22	42.95	43.09	43.11	43.96	43.88	...	...	...	...	...	0.297	0.302
19	2MASX J00341665-7905204	0.074000	0.022	0.033	0.082	0.152	...	...	...	...	...	...	...	(W,W,X,X,X)	44.41	44.46	44.44	44.44	...	...	...	...	...	...	...	0.490	0.491
20	2MASX J00343284-0424117	0.21300	0.001	0.003	0.010	0.027	...	...	...	...	...	...	...	(W,W,X,X,X)	44.19	44.45	44.51	44.69	...	...	...	...	...	...	...	0.219	0.226

Notes.— Infrared to X-ray properties of *Swift*/BAT 70-month AGN located at  $|b| > 10^\circ$ . (1) source No. in Baumgartner et al. (2013); (2) object name; (3) redshift; (4)–(14) IR flux density ( $f_\nu$ ) at 3.4, 4.6, 12, 22, 70, 90, 140, 160, 250, 350, and 500  $\mu\text{m}$  in units of Jy; (15) IR reference catalogs for 12  $\mu\text{m}$ , 22  $\mu\text{m}$ , 70  $\mu\text{m}$ , 90  $\mu\text{m}$ , and 160  $\mu\text{m}$ : A = AKARI PSC, H = Herschel/PACS, If = IRAS Faint Source Catalog, Ip = IRAS Point Source Catalog, W = WISE, X = Non Detection; (16)–(26) logarithmic IR luminosities ( $\log \lambda L_\lambda$ ) at 3.4, 4.6, 12, 22, 70, 90, 140, 160, 250, 350, and 500  $\mu\text{m}$  in units of  $\text{erg s}^{-1}$ ; (27)–(28) covering factor based on the correction of Stalevski et al. (2016) using the MIR information at 12 and 22  $\mu\text{m}$ , respectively. (This table is available in its entirety in the machine-readable format. A portion is shown here for guidance regarding its form and content.)

**Table 2.** Correlation Parameters between the IR and the 14–195 keV luminosity

Band	$N$	$\rho_L$	$\rho_f$	$P_L$	$P_f$	$a$	$b$
(1)	(2)	(3)	(4)	(5)	(6)	(7)	(8)
3.4	549	0.860	0.543	✓	✓	$0.000 \pm 0.028$	$0.890 \pm 0.030$
4.6	548	0.869	0.541	✓	✓	$-0.128 \pm 0.026$	$0.977 \pm 0.027$
12	596	0.815	0.547	✓	✓	$-0.099 \pm 0.024$	$0.963 \pm 0.022$
22	592	0.789	0.516	✓	✓	$0.024 \pm 0.024$	$0.979 \pm 0.022$
70	388	0.526	0.329	✓	✓	$0.235 \pm 0.035$	$0.943 \pm 0.036$
90	241	0.612	0.343	✓	✓	$0.407 \pm 0.032$	$0.904 \pm 0.035$
140	89	0.710	0.324	✓	✓	$0.683 \pm 0.045$	$0.867 \pm 0.045$
160	229	0.244	0.271	✓	✓	$0.098 \pm 0.044$	$0.884 \pm 0.046$
250	213	0.260	0.306	✓	✓	$-0.459 \pm 0.050$	$0.908 \pm 0.046$
350	170	0.417	0.277	✓	✓	$-0.788 \pm 0.050$	$0.821 \pm 0.060$
500	107	0.507	0.391	✓	✓	$-1.163 \pm 0.046$	$0.715 \pm 0.061$

Notes.— Correlation properties between 14–195 keV X-ray luminosity and infrared luminosities. (1) IR Band with a unit of  $\mu\text{m}$ ; (2) number of sample; (3) the Spearmans Rank coefficient for luminosity correlations ( $\rho_L$ ); (4) the Spearmans Rank coefficient for flux–flux correlations ( $\rho_f$ ); (5) the standard Student t-test null significance level for luminosity correlations ( $P_L$ ). ✓ represents  $P_L < 0.01$ ; (6) the standard Student t-test null significance level for flux–flux correlations ( $P_f$ ). ✓ represents  $P_f < 0.01$ ; (7) regression intercept ( $a$ ) and its  $1\sigma$  uncertainty; (8) slope value ( $b$ ) and its  $1\sigma$  uncertainty. Equation is represented as  $Y = a + bX$ .

**Table 3.** Equations of the luminosity correlation between the IR and X-Ray band

(1)	(2)	(3)	(4)	(5)	(6)	(7)	(8)
IR band	X-ray band	Equation	z range	$L_X$ range	Selection	AGN type	Reference
12 $\mu\text{m}$	14–195 keV	$\log \frac{L_{12\mu\text{m}}}{10^{43} \text{ erg/s}} = (-0.10 \pm 0.02) + (0.96 \pm 0.02) \log \frac{L_{14-195}}{10^{43} \text{ erg/s}}$	$z < 0.3$	$41 < \log L_{14-195} < 46$	X-ray	both	this study
22 $\mu\text{m}$	14–195 keV	$\log \frac{L_{22\mu\text{m}}}{10^{43} \text{ erg/s}} = (0.02 \pm 0.02) + (0.98 \pm 0.02) \log \frac{L_{14-195}}{10^{43} \text{ erg/s}}$	$z < 0.3$	$41 < \log L_{14-195} < 46$	X-ray	both	this study
12 $\mu\text{m}$	14–195 keV	$\log \frac{L_{12\mu\text{m}}}{10^{43} \text{ erg/s}} = (-0.21 \pm 0.03) + (1.05 \pm 0.03) \log \frac{L_{14-195}}{10^{43} \text{ erg/s}}$	$z < 0.3$	$43 < \log L_{14-195} < 46$	X-ray	both	this study
22 $\mu\text{m}$	14–195 keV	$\log \frac{L_{22\mu\text{m}}}{10^{43} \text{ erg/s}} = (-0.09 \pm 0.03) + (1.07 \pm 0.03) \log \frac{L_{14-195}}{10^{43} \text{ erg/s}}$	$z < 0.3$	$43 < \log L_{14-195} < 46$	X-ray	both	this study
6 $\mu\text{m}$	2–10 keV	$\log \frac{L_{12\mu\text{m}}}{10^{41} \text{ erg/s}} \simeq 2.1 \times 10^{-2} \left( 512 - \sqrt{2.2 \times 10^6 - 4.7 \times 10^4 \log \frac{L_{2-10}}{10^{41} \text{ erg/s}}} \right)$	$1.5 < z < 4.7$	$45 < \log L_{2-10} < 46.2$	optical	type-1	Stern (2015)
6 $\mu\text{m}$	2–10 keV	$\log \frac{L_{6\mu\text{m}}}{10^{43} \text{ erg/s}} = 0.40 + 1.39 \log \frac{L_{2-10}}{10^{43} \text{ erg/s}}$	$0.2 < z < 4$	$42 < \log L_{2-10} < 46$	X-ray	type-1	Fiore et al. (2009)
12 $\mu\text{m}$	2–10 keV	$\log \frac{L_{12\mu\text{m}}}{10^{43} \text{ erg/s}} = (0.19 \pm 0.05) + (1.11 \pm 0.07) \log \frac{L_{2-10}}{10^{43} \text{ erg/s}}$	$z < 0.1$	$41 < \log L_{2-10} < 45$	X-ray	both	Gandhi et al. (2009)
12 $\mu\text{m}$	2–10 keV	$\log \frac{L_{12\mu\text{m}}}{10^{43} \text{ erg/s}} = 0.30 + 0.99 \log \frac{L_{2-10}}{10^{43} \text{ erg/s}}$	$0.05 < z < 2.8$	$42 < \log L_{2-10} < 46$	X-ray	both	Mateos et al. (2015)
12 $\mu\text{m}$	2–10 keV	$\log \frac{L_{12\mu\text{m}}}{10^{43} \text{ erg/s}} = (0.33 \pm 0.04) + (0.97 \pm 0.03) \log \frac{L_{2-10}}{10^{43} \text{ erg/s}}$	$z < 0.3$	$40 < \log L_{2-10} < 46$	X-ray	both	Asmus et al. (2015)

Notes.— Correlation properties between 14–195 keV X-ray luminosity and infrared luminosities. (1) IR Band with a unit of  $\mu\text{m}$ ; (2) X-ray Band with a unit of  $\mu\text{m}$ ; (3) Equation of the luminosity correlation between IR and X-ray; (4) z range of the sample for each study; (5) X-ray luminosity range of the sample for each study; (6) The energy band used to select the parent AGN sample; (7) The main AGN type in the sample. “type-1” represents type-1 AGN, and “both” represents both type-1 and type-2 AGN; (8) Reference

**Table 4.** Standard Deviation of the IR to the expected slope

Sample	$N$	$\sigma$
(1)	(2)	(3)
3.4 $\mu\text{m}$ all	549	$0.3377 \pm 0.0204$
type-1	279	$0.3255 \pm 0.0276$
type-2	270	$0.3323 \pm 0.0287$
4.6 $\mu\text{m}$ all	548	$0.3544 \pm 0.0214$
type-1	281	$0.3339 \pm 0.0282$
type-2	267	$0.3617 \pm 0.0314$
12 $\mu\text{m}$ all	596	$0.3937 \pm 0.0228$
type-1	307	$0.3702 \pm 0.0299$
type-2	289	$0.4176 \pm 0.0348$
22 $\mu\text{m}$ all	592	$0.4266 \pm 0.0248$
type-1	302	$0.3941 \pm 0.0321$
type-2	290	$0.4572 \pm 0.0380$
70 $\mu\text{m}$ all	388	$0.5496 \pm 0.0395$
type-1	173	$0.5173 \pm 0.0558$
type-2	215	$0.5659 \pm 0.0547$
90 $\mu\text{m}$ all	241	$0.4665 \pm 0.0426$
type-1	87	$0.4566 \pm 0.0696$
type-2	154	$0.4727 \pm 0.0540$
140 $\mu\text{m}$ all	89	$0.4291 \pm 0.0647$
type-1	30	$0.4593 \pm 0.1206$
type-2	59	$0.4161 \pm 0.0773$
160 $\mu\text{m}$ all	229	$0.5860 \pm 0.0549$
type-1	100	$0.5816 \pm 0.0827$
type-2	129	$0.5906 \pm 0.0738$
250 $\mu\text{m}$ all	213	$0.6155 \pm 0.0598$
type-1	101	$0.5973 \pm 0.0845$
type-2	112	$0.6270 \pm 0.0842$
350 $\mu\text{m}$ all	170	$0.5316 \pm 0.0578$
type-1	75	$0.5245 \pm 0.0862$
type-2	95	$0.5362 \pm 0.0782$
500 $\mu\text{m}$ all	107	$0.4487 \pm 0.0616$
type-1	40	$0.4589 \pm 0.1039$
type-2	67	$0.4458 \pm 0.0776$

Notes.— (1) IR Band with a unit of  $\mu\text{m}$ ; (2) number of sample; (3) standard deviation ( $\sigma$ ) from the expected value  $L_{\text{IR}}^{(\text{slope})}$  given the slope in  $L_{\text{IR}}$  and  $L_{14-195}$ .